©Copyright 2017
Nao Murakami

High-Power Helicon Double Gun Thruster

Nao Murakami

A thesis submitted in partial fulfillment of the
requirements for the degree of

Master of Science

University of Washington

2017

Committee:

Robert M. Winglee

John D. Sahr

Program Authorized to Offer Degree:
Department of Aeronautics and Astronautics

University of Washington

Abstract

High-Power Helicon Double Gun Thruster

Nao Murakami

Chair of the Supervisory Committee:

While chemical propulsion is necessary to launch a spacecraft from a planetary surface into space, electric propulsion has the potential to provide significant cost savings for the orbital transfer of payloads between planets. Due to extended wave particle interactions, a plasma thruster that can operate in the 100 kW to several MW power regime can only be attained by increasing the size of the thruster, or by using an array of plasma thrusters. The High-Power Helicon (HPH) Double Gun thruster experiment examines whether firing two helicon thrusters in parallel produces an exhaust velocity higher than the exhaust velocity of a single thruster. The scaling law that relates the downstream plasma velocity with the number of helicon antennae is derived, and compared with the experimental result. In conjunction with data analysis, two digital filtering algorithms are developed to filter out the noise from helicon antennae. The scaling law states that the downstream plasma velocity is proportional to square root of the number of helicon antennae, which is in agreement with the experimental result.

TABLE OF CONTENTS

LIST OF FIGURES

LIST OF TABLES

ACKNOWLEDGMENTS

Thank you to...

Professor Robert Winglee for guidance in HPH research, serving on the committee, and the many out-of-the-box ideas that keep the Advanced Propulsion Laboratory (APL) going.

Professor John Sahr for moral support, helpful advice, serving on the committee, and assisting many APL research projects.

Professor Nathan Kutz for the Data Analysis course that greatly helped in developing the digital filtering algorithm.

Professor Erika Harnett for being a role model and mentor, teaching me what leadership looks like through example, and inexhaustible witty banter.

(Soon-to-be Dr.) Juan Carlos Chavez for being a mentor, and along with Professor Harnett, connecting me with many outreach opportunities that were crucial in developing scientific communication skills.

Professor Mason Peck (from Cornell University) for continued support and mentorship, and for encouraging me to pursue graduate studies in plasma propulsion.

Eagle Harbor Technologies, Inc. for their continued support for APL, and especially for all of the guidance in developing the power supplies for the Double Gun system.

The APL members, past and present, for assistance in running (and troubleshooting) the Double Gun thruster experiment, developing diagnostics, moral support, and (mostly good) playlist selection.

Beth Boardman, for being my geeky best friend with shared appreciation of good TV, movies, books, and music.

Peter Norgaard, for being my math wizard husband with excellent taste in soccer.

Mia San Mia

Chapter 1

HISTORY OF HELICON

Helicon wave creates high density plasma ($\sim 10^{-18} m^{-3}$) through radio frequency heating, and it known to have high ionization efficiency. Helicon wave a radially confined whistler wave.

Whistler wave is a low frequency electromagnetic wave that can be observed in naturally occurring plasma – lightning. Earliest record of whistler wave observation dates back to World War I. During the war, amplifier was used to listen in on the enemy communications, through which soldiers have reported to have listened "a very remarkable whistling note" in the telephone lines. In 1930, Barkhausen offered two explanations on how the "whistling note" propagates from the source to a distant location where the said "whistling note" is observed.[7] One is that the electromagnetic impulse caused by a lightening stroke travels along the earth through continuous reflection between atmosphere and ground. Another is that the wave is traveling through the earth. While he was unable to provide a solid conclusion, he correctly deduced the relationship between whistler wave and lightning, and notes in several places that the observation of whistler wave is closely tied to "strong atmospheric disturbances," or thunderstorms.

1.1 Early Years

Helicon wave propagates through plasma in the presence of magnetic field. Helicon wave has a frequency that is greater than ion cyclotron frequency, and less than electron cyclotron frequency. In other words, electrons will be affected by the helicon wave, and ions will remain unaffected by the helicon wave. This is because ions do not oscillate fast enough to see the effect of the helicon wave.

$$\omega_{ci} \ll \omega_{helicon} \ll \omega_{ce} \tag{1.1}$$

The objective of Lehane and Thonemann's 1965 experiment was to validate the helicon theory by studying helicon wave propagation in a radially confined plasma.[8] Lehane and Thonemann compared their experimental results with Klozenberg, MacNamara, and Thonemann's helicon wave propagation theory in cylindrical plasma.[9] To summarize, Helicon wave creates perturbation in the magnetic field of the form, expressed in cylindrical coordinate:

$$\mathbf{B_w} = \mathbf{B_0} exp[i(k_z z + m\theta - \omega t)] \tag{1.2}$$

Lehane and Thonemann studied the case where the azimuthal wave number, m, equals 0 and +1. The azimuthal wave number corresponds to the wave rotation. +1 and -1 corresponds to right and left handed rotation of the wave with respect to the base magnetic field. The experimental results for wave dispersion, attenuation, and $\mathbf{B_w}$ structure as a function of radius were all in agreement with the theory. The one region where the experimental results did not agree was the boundary region, where the theoretical results did not account for non-uniform electron density.

In 1984, Boswell studied the helicon wave further and discovered that plasma can be produced by coupling radio frequency (RF) power near lower hybrid frequency with standing whistler wave.[10] From experimentations, he concluded that 50% of the RF power to plasma is lost due to discharge, and other 50% goes into ionization and excitation of the gas. He also observed that as the axial magnetic field was increased from 100G to ∼500G, the plasma density increased by five times its previous value, and the color of the plasma turned from light pink (neutral Ar) to light blue (Ar_2).

In 1991, Chen derived the following dispersion relation for helicon wave in a uniform, bounded plasma.[11]

$$\frac{\omega}{k} = \frac{3.83}{a}\left(\frac{B_0}{\mu_0 e n_0}\right) \tag{1.3}$$

This dispersion relation shows that three factors contribute to the phase velocity of the helicon wave: base magnetic field strength, plasma density, and the antenna diameter. The base magnetic field strength is proportionally related to the phase velocity, while plasma density and antenna diameter is inversely proportional to the phase velocity. Chen also discussed whether the damping on helicon wave is dominated by collisional damping or Landau damping. By comparing the electron-ion collision frequency to Landau damping frequency, he derived the following break-even condition where $\nu_{\text{LD}} = \nu_{ei}$.

$$n_e = 2.6 \times 10^{11}\omega = 1.63 \times 10^{12} f \tag{1.4}$$

For a given frequency, Landau damping will be the dominant damping mechanism when the plasma density is at or below the value obtained from equation 1.4.

In 1994, Light and Chen compared three types of Nagoya type III antennae as shown below, and found out that right-handed polarization was preferentially excited by all three types of antennaeċitelight1995helicon

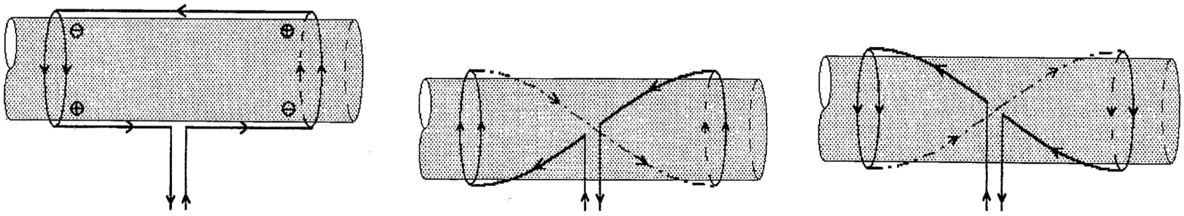

(a) Nagoya Type III (b) Right-handed helical (c) Left-handed helical

Figure 1.1: Antenna types used in helicon experiment[1]

Figure 1.1(a) is the plane polarized Nagoya Type III antenna. Figures 1.1(b) and 1.1(c) are Nagoya Type III antennae with 180° helical twist. Looking in the direction of the wave propagation, if the antenna leads twist in the counterclockwise direction, then the antenna is right-handed. If the antenna leads twist in the clockwise direction, then the antenna is left-handed. This is not to be confused with the rotational direction for the helicon **wave**, which is represented by $m = +1$(right-handed) and $m = -1$ (left-handed). The rotational direction of the helicon wave is determined with respect to the direction of the base magnetic field, $\mathbf{B_0}$. The relationship between the helicity of the antenna and the wave with $\mathbf{B_0}$ is tabulated below.

Table 1.1: Relationship between the helicon antenna and wave helicities

	Helicon Wave	
Helicon Antenna	Parallel to $\mathbf{B_0}$	Antiparallel to $\mathbf{B_0}$
Right Handed	Right Handed Wave	Left Handed Wave
Left Handed	Left Handed Wave	Right Handed Wave

Light and Chen were successfully able to excite $m = +1$ mode in all configurations, including plane polarized antenna. Interestingly, they were not able to excite $m = -1$ configuration, even on the antenna and $\mathbf{B_0}$ configuration that is designed to excite $m = -1$ configuration. They hypothesized that the left-handed polarization mode required higher peak plasma density than was achievable in their experimental setup.

Helicon as a plasma source can be applied to space propulsion; however, it also has applications other than space propulsion. Perry et al. noted that helicon can produce high-density plasma, and suggested application to semiconductor processing in the form of pulsed plasma etching.[12] Through experimentation, Loewenhardt et al. demonstrated the use of helicon to generate a relatively dense plasma in toroidal confinement devices.[13] This experiment showed promising results to verify the previous theory by Chen that the high ionization efficiency is due to Landau damping.[11]

1.2 Application to Space Propulsion

1.2.1 Current-Free Helicon Double Layer Thruster

In 2004, Charles and Boswell published the experimental studies on Current-free Helicon Double Layer Thruster (HDLT).[2] The theoretical aspect of current-free double layers was further investigated by Chen.[14] HDLT accelerates ions through a current-free double layer, which is a voltage drop that forms downstream of the plasma source, and at a boundary between plasmas with two different thermal temperatures. In order for this phenomenon to take place, the magnetic field has to be aligned with the electric field, which is most commonly observed in the auroral plasma. Helicon antenna that is 15cm in diameter and 20cm in length is used as a plasma source. The antenna is tuned to a frequency of 13.56MHz, and the two solenoids are placed around the antenna to create a magnetic field of approximately 250G in the source region. The background chamber pressure is set at 2×10^{-6}torr, and Argon is used as a propellant. The retarding field energy analyzer is used to measure the ion velocity 12cm downstream of the double layer.

The measured beam velocity yielded $2c_s$ (speed of sound), or 681 m/s. As shown in figure 1.2, the ion beam profile was obtained in order to visualize the plasma behavior in the double layer. Because the diameter of the ion beam roughly corresponds to the diameter of the antenna, it can be inferred that the ion beam is not strongly affected by the expanding magnetic field. In 2006, Charles et al made several changes to the HDLT parameters.[15] The background chamber pressure was lowered to 2×10^{-7}torr, while the RF power was increased to 500W. Also, the type of propellant being used was changed from Argon to Xenon. As a result of these changes, the beam velocity increased to 6 km/s.

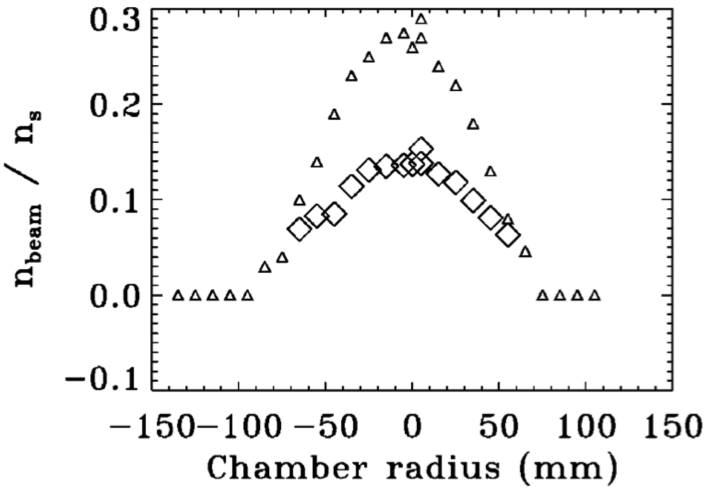

Figure 1.2: Density ratio (diamonds) across the chamber radius, and theoretical upper limit of the density ratio (triangles)[2]

1.2.2 VASIMR®

The earliest publication of Variable Specific Impulse Magnetoplasma Rocket (VASIMR®) dates back to 1997. In 2001, Diaz published a detailed overview of VASIMR®, encompassing theoretical background, engineering design, laboratory experiment, and application to space mission.[16] VASIMR® is a three-stage thruster. First stage uses a helicon source to ionize gas (Helium, Hydrogen, Deuterium, or mixture of these) through RF heating and create plasma. Second stage accelerates ion through ion cyclotron resonance heating (ICRH). Third stage used magnetic nozzle to achieve high exhaust velocity of the plasma through adiabatic expansion. As the name suggests, VASIMR® is able to vary its specific impulse, allowing for flexible adjustments in accordance with the orbital characteristics on any given mission. Variable specific impulse is achieved by changing the power input to helicon and ICRH system. For high thrust, the power is predominantly directed to the helicon, whereas for high specific impulse, more power is directed to the ICRH system.

There are several VASIMR® prototypes built to this date. The initial prototype, VX-50, was decommissioned and disassembled in October 2006, and replaced with VX-100 and

VX-200. VX-100 is designed as a laboratory physics demonstrator test bed, and VX-200 is a flight-like prototype. VF-200, a space-flight test model, is expected to follow.

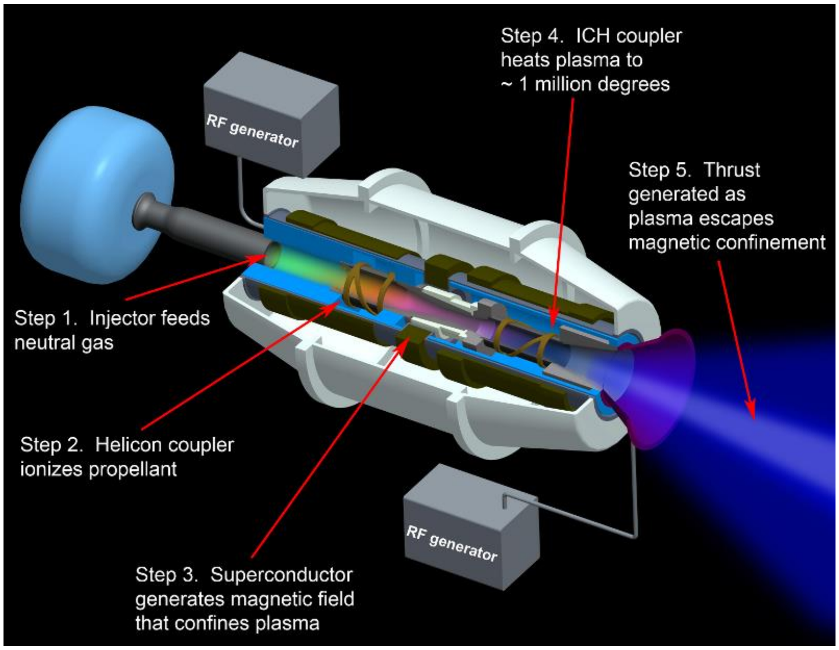

Figure 1.3: Schematic of the VASIMR® VX-200[3]

In 2014, Bering et al. conducted the VX-200 testing in a 150m^3 vacuum chamber with the background chamber pressure of 1×10^{-4}torr.[3] A plasma momentum flux sensor (thrust stand) was used to characterize the exhaust plume over the range of 5m in the axial direction and 1m in the radial direction. Maximum thrust of around 6N was obtained at 200kW RF power. The results also indicated the maximum exhaust velocity to be around 50 km/s with maximum thruster efficiency of 72%. The application of VASIMR® to the Europa orbiter mission was proposed, where the travel time was reduced from 6 years (through conventional gravity assists) to 3 years with VASIMR®.

1.2.3 Other Helicon Thruster Research

There are several other propulsion research that uses helicon antenna as a plasma source. A few institutions are in the process of developing an innovative helicon thruster. Around

2010, University of Maryland started to develop a helicon thruster using superconducting magnets. There are no experimental results for this thruster to be discussed as of yet. In 2012, Vitucci and Sedwick presented the theory and superconductor alignment simulation results, and the use of magnetic mirror to increase the thruster efficiency is proposed.[17] In 2014, Sheehan et al. presented the preliminary study and prototype of the helicon thruster that is miniaturized to fit onto a CubeSat.[18] Helicon antenna that is approximately 3.5cm in length was 3D printed out of solid silver. The proposed mass budget of the thruster is 0.5kg; however, this does not include the RF power supply nor the propellant. The proposed power budget for the thruster is 50W. Both mass and power will be an issue that needs resolving before the thruster is successfully implemented on a CubeSat design. It is of interest to see how these two thruster concepts develop in the years to come.

1.3 High-Power Helicon Thruster

High-Power Helicon (HPH) thruster has been extensively researched at University of Washington's Advanced Propulsion Laboratory since the early 2000's. The concept of HPH thruster originated from the Mini-Magnetospheric Plasma Propulsion (M2P2).[19] The M2P2 creates a magnetosphere having a radius of 15-20 km around the spacecraft, which would then generate propulsion by deflecting solar wind particles. Because the magnetic field decreases as $1/r^3$, plasma is injected in the system to expand the magnetic field. Once the plasma moves into a regime where the plasma pressure exceeds magnetic pressure, plasma is able to push the magnetic field outwards. The proposed prototype has three components: a strong ($\sim$700G) magnetic field on the spacecraft, a plasma source to inflate the magnetic field, and a power source in the kW regime to generate both the magnetic field and plasma. From theoretical analysis, the M2P2 would be able to accelerate a 70-140 kg spacecraft to 50-80 km/s.

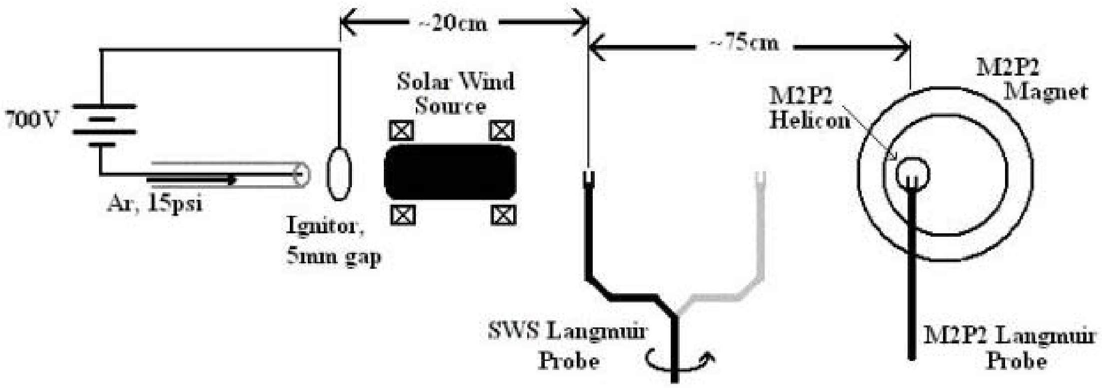

Figure 1.4: Schematic of the M2P2 prototype[4]

As shown in figure 1.4, helicon antenna was used as a plasma source to demonstrate the creation of the smaller scale magnetosphere in a laboratory setting. Ziemba et al. demonstrated in 2003 that helicon source in the M2P2 prototype can operate near 100% ionization efficiency at optimal gas puff parameters.[20] Plasma density near helicon source region increased as the input power was increased. This characteristic, combined with the high ionization efficiency, gave inspiration to adapt the M2P2 prototype to High-Power Helicon (HPH) thruster.

HPH thrusters operate at a frequency range of 500 kHz to 1MHz, which is much lower than other helicon experiments discussed thus far. This is achieved by the development of solid-state power supply that is capable of switching at high currents (>100A) at frequencies in the order of MHz.[21] There are several advantages to operate helicon thruster at the low frequency regime:

1. High electrical efficiency when RF power is generated at low frequencies
2. High RF power (10s of kW), which yields high thruster efficiency and high specific impulse
3. Reduced magnetic field strengths when compared with the conventional magnetic coils used for helicon thrusters, consequently reducing the overall mass of the system

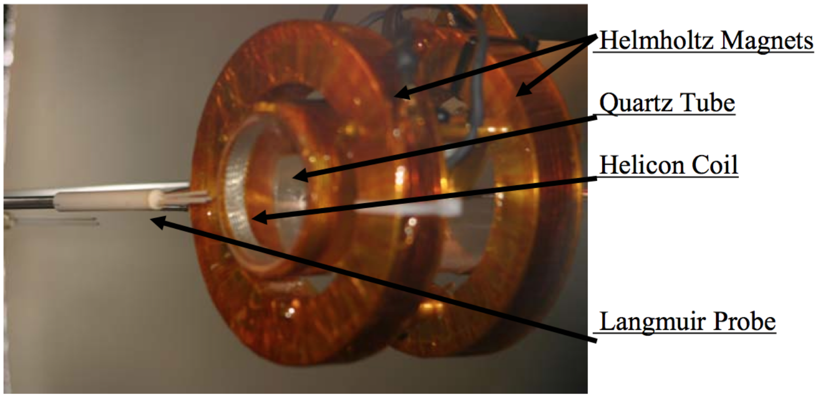

Figure 1.5: HPH thruster prototype[5]

In 2005, Ziemba et al. built the prototype of HPH thruster (figure 1.5) and collected data to characterize its baseline performance.[5] The chamber background pressure was kept at $1{\times}10^{-5}$torr or lower. The peak plasma density was measured to be $2 \times 10^{20}\mathrm{m}^{-3}$, which proved to be more than an order of magnitude higher than other helicon experiments. The addition of DC magnetic field with strength of 150G resulted in successful collimation of the beam. The time of flight data was taken by placing two Langmuir probes downstream of the exhaust plasma flow. Argon and Hydrogen gasses were used as propellants, and yielded an exhaust velocity of around 20 km/s and 50 km/s, respectively. By changing the RF power input to the helicon antenna, a direct correlation was shown between the RF power and the exhaust velocity of the plasma.

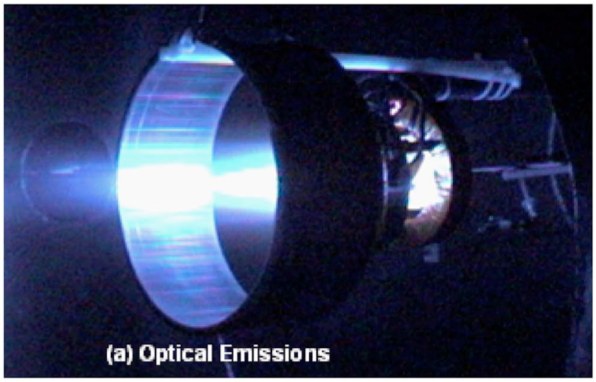

Figure 1.6: HPH thruster with two downstream nozzles[6]

Later, the addition of magnetic nozzles downstream of the helicon antenna (figure 1.6) was proposed by Winglee et al. to provide collimation of the plasma.[6] This was verified both through computer simulation and experiment. The addition of magnetic nozzle makes the plasma super-Alfvénic, which means that the flow of the plasma is faster than the Alfvén speed. Since Alfvén speed is dependent on magnetic field strength, this consequently means that the plasma pressure is larger than magnetic pressure. The plasma particles detach from the magnetic field lines, and self-collimate due to the induced magnetic field created by the plasma particles itself. The beam collimation was even furthered with the addition of the second nozzle to the system. Overall, this enhances the performance of HPH thruster through two aspects:

1. Increase the efficiency of the HPH thruster by converting the thermal energy to directed energy
2. Increase the plasma density downstream, thus increasing the thrust and specific impulse of the HPH thruster

In 2008, Prager et al. measured the ion energy downstream of the helicon antenna to confirm that the helicon antenna directly affects the acceleration of plasma downstream of the source region.[22] The chamber background pressure is kept at 1×10^{-6}torr, and Argon gas was used as a propellant. Using the Retarding Energy Field Analyzer (REFA), the ion velocity distribution functions were obtained at 20, 40, and 50cm downstream from the source region. The average ion energy was shown to be higher at 40cm than at 20cm, which indicates that the ion velocity increased downstream. This increase in velocity is due to the helicon wave propagation downstream. In the downstream region, ions are not magnetized; however, electrons are magnetized. The charge imbalance between electrons and ions result in an ambipolar electric field that results in the ion acceleration. This was verified by Prager et al. in 2010, by measuring the magnetic field perturbations downstream using B-dot probes.[23] The expansion rate of the helicon wave is comparable to the expansion rate of magnetic field lines. In other words, the helicon wave follows the magnetic field lines as they transition into the area downstream of the source region. This also implies that the helicon wave is radially bounded by the magnetic field geometry in the downstream region.

In 2011, Roberson et al. changed the antenna from the previously used right-handed Nagoya type III helical antenna to left-handed Nagoya type III helical antenna.[24] This increased the helicon antenna current driven downstream of the plasma flow, which correlated with the increased diamagnetic perturbation downstream. The results suggested that if the current driven downstream can be increased, the beam collimation will extend further from the HPH thrusters, thus increasing the thruster efficiency. Later on, Roberson added a larger left-handed Nagoya type III helical antenna downstream, where the diameter of the antenna was doubled.[25] As a result of this addition, both the increased ion velocity and improved beam collimation were observed.

1.4 High-Power Helicon Double Gun Thruster

The HPH Double Gun thruster uses two left-handed Nagoya type III helical antennae and thrusters in parallel. The previous studies discussed in this chapter have shown that there is a direct correlation between the power input to the helicon antenna and the exhaust velocity of the plasma. The area that has not been explored yet is whether the interaction of the two plasma streams enhances the efficiency of the overall system. The performance of the HPH Double Gun thruster is compared to the single HPH thruster.

The addition of another HPH thruster to the system resulted in the duplication of all of the associated electronics. The antenna power supply was upgraded and rebuilt with significant assistance from Eagle Harbor Technologies, Inc., as the existing power supplies were incapable to withstand being operated simultaneously. Also, the impedance for the two thrusters had to be matched, so that both antennae can be tuned at the same frequency.

Langmuir probe was used to collect the plasma profile downstream of the HPH Double Gun thruster, and was also used to collect the time of flight data. The initial findings suggest that there are positive interaction between two helicon antennae, resulting in the increased exhaust velocity when the two HPH thrusters are simultaneously fired side-by-side.

Chapter 2

HELICON THEORY

Helicon wave has the frequency that is higher than ion cyclotron frequency, but less than electron cyclotron frequency. In other words, electrons will be affected by the helicon wave, and ions will remain unaffected by the helicon wave. This is because ions do not oscillate fast enough to see the effect of the helicon wave. For HPH Double Gun thruster, the helicon antenna, electron cyclotron, and ion cyclotron frequencies near the antenna source region compare as tabulated below. The decrease in the total magnetic field is due to the diamagnetic perturbation that happens around 30cm (1λ) downstream from the source region.[25]

$$\omega_{ci} \ll \omega_{antenna} \ll \omega_{ce} \tag{2.1}$$

Table 2.1: Comparison of helicon antenna, electron cyclotron, and ion cyclotron frequencies with various magnetic field downstream

Distance from Helicon Antenna	Magnetic Field [G]	$\omega_{ci}[\frac{rad}{s}]$	$\omega_{antenna}[\frac{rad}{s}]$	$\omega_{ce}[\frac{rad}{s}]$
source region	400	9.64×10^4	3.93×10^6	7.03×10^9
30cm (1λ)	10	2.41×10^3	3.93×10^6	1.76×10^8
60cm (2λ)	2	482	3.93×10^6	3.52×10^7

From previous studies by Prager, it has been shown experimentally that the plasma particles are accelerated downstream of the source region.[22] This acceleration is attributed to the ambipolar electric field due to charge imbalance between electron and ions. In the source region, the helicon wave inputs energy into the gas through RF heating, and ionizes the gas. The base magnetic field coils create a $\mathbf{j} \times \mathbf{B}$ force, which restricts the radial motion of the particles and collimates the beam. In the source region, electrons are magnetized, and ions are weakly magnetized.

In the region downstream of the HPH Double Gun thruster, the perturbation in the magnetic field due to helicon wave propagation causes the particle to further ionize and accelerate via ambipolar electric field. Electrons travel faster than ions, therefore, there is no charge neutrality. From Gauss's law, electric field develops in between electrons and ions, and the two species are pulled together. This motion results in increased ion velocity, and as a result, an increase in the bulk velocity downstream of the thruster.

The dispersion relation for the source region is derived by Chen.[11]

$$\frac{\omega}{k} = \frac{3.83}{a}\left(\frac{B_0}{\mu_0 e n_0}\right) \tag{2.2}$$

The above equation shows that three factors contribute to the phase velocity of the helicon wave: base magnetic field strength, plasma density, and the antenna diameter. The base magnetic field strength is proportionally related to the phase velocity, while plasma density and antenna diameter is inversely proportional to the phase velocity. This equation is valid as long as the plasma is confined within the helicon antenna. Once the plasma exits the source region in a form of a thruster, it is no longer bounded, making the above dispersion relation is not applicable. A separate dispersion relation for a whistler wave needs to be derived to accurately describe the plasma downstream of the HPH Double Gun thruster.

The derivation below discusses the plasma particle behavior **downstream** of the HPH Double Gun Thruster. First, we assume the helicon wave perturbation takes the form of:

$$n_1 = \|n\| exp[i(kx - \omega t + m\theta)] \tag{2.3}$$

Lorentz force equation is expressed as:

$$\mathbf{F} = m\frac{d\mathbf{v}}{dt} = q\mathbf{E} + q\mathbf{v} \times \mathbf{B} \tag{2.4}$$

with the following perturbation terms, denoted with a subscript 1.

$$\mathbf{v} = \mathbf{v_0} + \mathbf{v_1} \tag{2.5}$$

$$\mathbf{E} = \mathbf{E_0} + \mathbf{E_1} \tag{2.6}$$

$$\mathbf{B} = \mathbf{B_0} + \mathbf{B_1} \tag{2.7}$$

Substituting the perturbation terms into equation 2.4 gives us:

$$m\frac{d}{dt}\left(\mathbf{v_0} + \mathbf{v_1}\right) = q\left(\mathbf{E_0} + \mathbf{E_1}\right) + q\left(\mathbf{v_0} + \mathbf{v_1}\right) \times \left(\mathbf{B_0} + \mathbf{B_1}\right) \tag{2.8}$$

$\mathbf{v_0}$ and $\mathbf{E_0}$ are 0, because the system does not have initial velocity nor electric field. Expanding the above equation gives:

$$m\frac{d\mathbf{v_1}}{dt} = q\mathbf{E_1} + q\left(\mathbf{v_1} \times \mathbf{B_0} + \mathbf{v_1} \times \mathbf{B_1}\right) \tag{2.9}$$

The term $\mathbf{v_1} \times \mathbf{B_1}$ is negligible as it is a product of two perturbation terms. The Lorentz force equation with helicon wave perturbation is simplified to:

$$m\frac{d\mathbf{v_1}}{dt} = q\mathbf{E_1} + q\mathbf{v_1} \times \mathbf{B_0} \tag{2.10}$$

Now, let the phase variable ϕ is defined as $kx - \omega t + m\theta - \pi$. The $-\pi$ term is added in order to shift the phase as to declutter the following equations of minus signs. The first and second derivatives of ϕ with respect to time are:

$$\frac{d\phi}{dt} = k\frac{dx}{dt} - \omega + m\frac{d\theta}{dt} \tag{2.11}$$

$$\frac{d\phi^2}{d^2t} = k\frac{dv}{dt} + m\frac{d\theta^2}{d^2t} \tag{2.12}$$

The second derivative of θ with respect to time is 0, since the helical motion of the helicon wave is not accelerating. Assume that the electric potential has a form:

$$\mathbf{V_{E1}} = \|\mathbf{V_{E1}}\| cos(kx - \omega t + m\theta) \tag{2.13}$$

Which then becomes:

$$\mathbf{E_1} = -\nabla \mathbf{V_{E1}} \tag{2.14}$$

$$\mathbf{E_1} = k\|\mathbf{V_{E1}}\| sin(kx - \omega t + m\theta) \tag{2.15}$$

Therefore, equation 2.10 can be rewritten as:

$$\frac{d\mathbf{v_1}}{dt} = \frac{q}{m}\left(k\|\mathbf{V_{E1}}\| sin\phi + \|\mathbf{v_1}\|\|\mathbf{B_0}\| sin\phi\right) \tag{2.16}$$

Combining equation 2.16 with 2.12 and substituting $\|\mathbf{V_{E1}}\| = \frac{\|\mathbf{E_1}\|}{\mathbf{k}}$ gives:

$$\frac{d^2\phi}{dt^2} = \frac{qk}{m}\left(\|\mathbf{E_1}\| + \|\mathbf{v_1}\|\|\mathbf{B_0}\|\right) sin\phi \tag{2.17}$$

As this takes the form of the non-linear pendulum equation, the trapping frequency for the particle in whistler wave downstream of the source can be written as:

$$\omega_t^2 = \frac{qk}{m}\left(\|\mathbf{E_1}\| + \|\mathbf{v_1}\|\|\mathbf{B_0}\|\right) \tag{2.18}$$

Rearranging the above equation, the dispersion relation for the whistler wave is:

$$\frac{\omega_t}{k} = \sqrt{\frac{q}{mk}\left(\|\mathbf{E_1}\| + \|\mathbf{v_1}\|\|\mathbf{B_0}\|\right)} \tag{2.19}$$

The wave trapping theory states that electrons are **trapped** by the wave if the trapping frequency is greater than the resonance frequency.[26] A simple visualization of wave trapping is that electrons would get trapped in the trough of a sinusoidal wave. The trapped electrons oscillate in the potential trough with the trapping frequency, ω_t. The electric field term in equation 2.18 can be expressed in terms of magnetic field perturbation $\mathbf{B_1}$ by applying perturbation theory to Faraday's Law. The resulting expression is:

$$\|\mathbf{E_1}\| = \frac{\omega\|\mathbf{B_1}\|}{k} \tag{2.20}$$

The above expression is substituted into equation 2.18, and the mass of the particle is specified as that of an electron. The wave number, k, is the magnitude of $k_{\|}$ and $k_{\perp}$.

Because the wave is propagating in the parallel direction, $k_{\parallel}$ is taken to be the dominant direction and thus will have a value much greater than $k_{\perp}$. Equation 2.18 then becomes:

$$\omega_t^2 = \frac{qk_{\parallel}}{m_e}\left(\frac{\omega\|\mathbf{B_1}\|}{k_{\parallel}} + \|\mathbf{v_1}\|\|\mathbf{B_0}\|\right) \tag{2.21}$$

The following values are substituted into equation 2.21: wave number $k_{\parallel} = \frac{2\pi}{0.3m}$, helicon wave frequency $\omega = 3.93 \times 10^6 \frac{rad}{s}$, magnetic field perturbation $\|\mathbf{B_1}\| = 0.001T$, electron thermal velocity $\|\mathbf{v_1}\| = 1.88 \times 10^6 \frac{m}{s}$, and base magnetic field $\|\mathbf{B_0}\| = 0.01T$.[25] These values are taken at approximately 30cm (1λ) downstream from the source region. Comparison of the order of magnitude between $\frac{\omega\|\mathbf{B_1}\|}{k_{\parallel}}$ and $\|\mathbf{v_1}\|\|\mathbf{B_0}\|$ shows that electron thermal velocity, $\|\mathbf{v_1}\|$, is the driving factor in making the $\|\mathbf{v_1}\|\|\mathbf{B_0}\|$ the dominant term. The trapping frequency is therefore:

$$\omega_t = 2.64 \times 10^8 \frac{rad}{s} \tag{2.22}$$

The resonance condition for whistler wave is expressed as:

$$\Delta\omega = |\omega - \omega_{ce} + k_{\parallel}v_{\parallel}| \tag{2.23}$$

The following values are substituted into equation 2.23: helicon wave frequency $\omega = 3.93 \times 10^6 \frac{rad}{s}$, downstream electron cyclotron frequency $\omega_{ce} = 1.76 \times 10^8 \frac{rad}{s}$, wave number $k_{\parallel} = \frac{2\pi}{0.3m}$, and electron thermal velocity $v_{\parallel} = 1.88 \times 10^6 \frac{m}{s}$. These values are also taken at approximately 30cm (1λ) downstream from the source region. The resonance frequency is:

$$\omega_{res} = 1.33 \times 10^8 \frac{rad}{s} \tag{2.24}$$

The trapping frequency is greater than the resonance frequency, which satisfies the particle trapping condition. Equation 2.19 supports the theory that the velocity of the HPH Double Gun thruster would be higher than the average of Right and Left Guns fired individually. When the HPH Double Gun thruster is fired, $\mathbf{E_1}$ and $\mathbf{v_1}$ would be doubled. Therefore, the downstream velocity for the Double Gun would be $\sqrt{2}$, or 41% faster than the average of

Right and Left Guns fired individually. The scaling law for the HPH thruster array can be extrapolated to cases where more than 2 helicon antennae are used.

$$\text{Downstream Velocity} \propto \sqrt{\text{Number of Helicon Antenna}} \tag{2.25}$$

As indicated by the above scaling law, the downstream velocity increases by 41% for 2 helicon antennae and 73% for 3 helicon antennae. For the downstream velocity to double and triple, 4 and 9 helicon antennae are required, respectively. This scaling law can be used to evaluate the trade-off between the benefit of increased downstream velocity and the increased power input that corresponds with the increased number of antennae.

Chapter 3

EXPERIMENTAL SETUP

This chapter describes the details of the High-Power Helicon (HPH) Double Gun thruster experimental apparatus, and the vacuum chamber that houses the thruster.

3.1 Vacuum Chamber

HPH Double Gun thruster is placed at one end of a 4800L stainless steel vacuum chamber that is approximately 2.7m in length and 1.5ft in diameter. Facing into the vacuum chamber (figure 3.1(a)), the flanges on the right allows for diagnostic probes, such as Langmuir and Retarding Energy Field Analyzer (REFA) probes, to be inserted and moved radially. The window flanges on the left allows for the visual data collection by utilizing high-speed CCD camera. A track is placed on the ceiling of the chamber, allowing for probes, such as B-Dot probes, to be suspended and moved axially. The details of the diagnostics will be discussed further in the following chapter.

In order to achieve vacuum, first a roughing pump is turned on, which lowers the chamber pressure to 500mTorr. At which point, a turbo pump (Varian Turbo-V 551 Navigator) is turned on to further lower the pressure to 10^{-6}Torr range. At a pressure above 1-2$\times10^{-4}$Torr, two Pirani gauges are used to monitor the chamber pressure. Below that pressure, a glass tube Bayard-Alpert ion gauge is turned on.

3.2 HPH Double Gun Thruster System

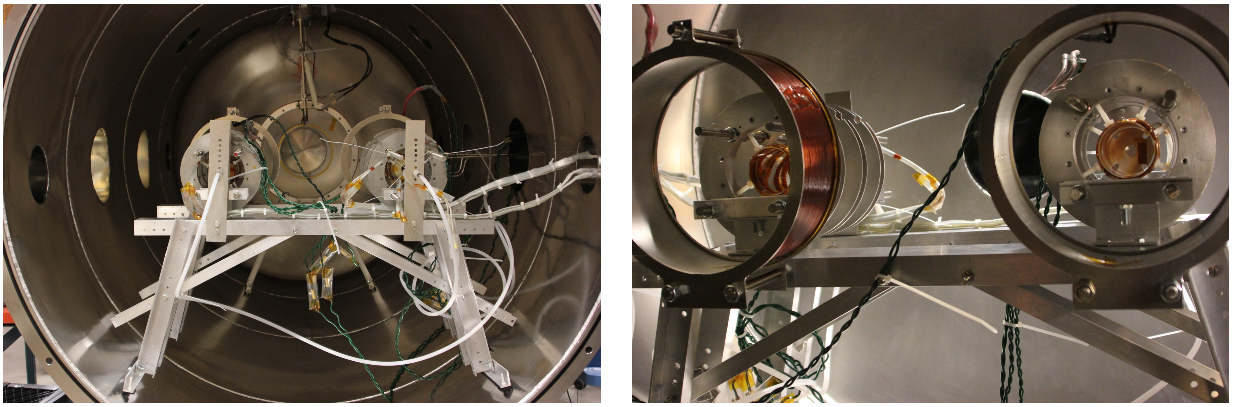

(a) Back view

(b) Front view

Figure 3.1: Double Gun experimental setup

Figure 3.1 shows the Double Gun thruster inside of the vacuum chamber. The chamber pressure is maintained at 10^{-6} torr range over the course of data collection. Facing into the vacuum chamber (figure 3.1(a)), the thruster to the left is referred to as the Left Gun and the thruster to the right is referred to as the Right Gun. Each thruster is 40cm in length, and the distance between the centerline of Right and Left Guns are 50cm. Each thruster uses a Nagoya type III helical antenna, and is made from a quartz tube that is 15cm long. Three base field magnetic coils are placed around each helicon antenna to direct the plasma, and have inner diameter of 13cm. The magnetic nozzle is placed 11cm downstream from the base field magnetic coils to eject the plasma from the antenna, and has inner diameter of 25cm. The stand that the Double Gun thrusters are mounted on is designed to allow the base magnets to change its yaw angle. In this case, two thrusters are angled at approximately 15° toward each other, ensuring that the exhaust plasma from the two thrusters interact with each other. HPH thrusters use noble gases as a propellant. In this particular experiment, Argon gas is used because in addition to its affordability and stable nature, it does not erode the experimental apparatus in the vacuum chamber. Each thruster is equipped with its own gas puff system, igniter, and helicon antenna power supply allowing for fine calibration of the thruster performance parameters.

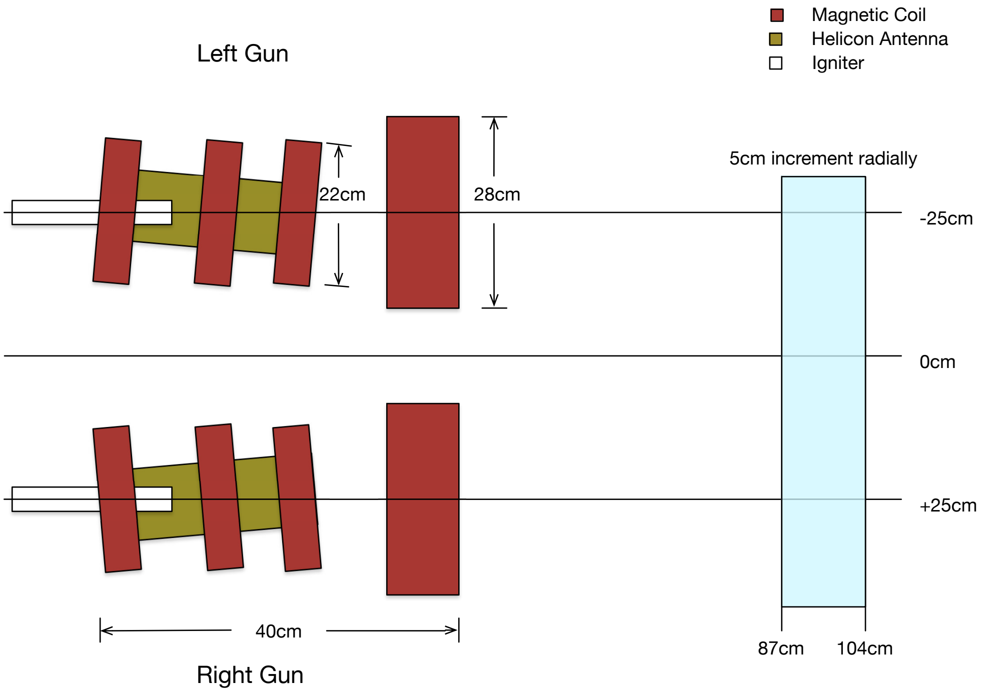

Figure 3.2: Schematic of the Double Gun experimental setup

Figure 3.2 summarizes the experimental setup in a simple schematic. A gas puff valve and control circuit system allows small amount of Argon gas to be puffed into a quartz tube. An igniter at the end of the gas puff system creates a seed plasma. Then, a helicon antenna is turned on to ionize the Argon gas inside of a quartz tube. Base field magnetic coils and a magnetic nozzle is used to direct the plasma out of a quartz tube, completing one thruster firing cycle. Due to the angling of the thruster by 15° toward each other, most of the data is collected at axial location of 87cm and 104cm, measured from the plasma ejection end of the quartz tube. Radial sweep was done at 5cm increment. From basic trigonometry, it has been estimated that this location is roughly the region where the two beams from the Double Gun thruster most interact with one another.

3.3 Neutral Gas Injection and Igniter

Both the chamber condition and the Double Gun thruster firing duration are optimized to simulate space-like environment. Background neutral pressure is kept in the order of mid-to-low 10^{-6}Torr range. The Argon gas is puffed in for 4-9 ms, ensuring that the chamber is not backfilled with Argon. The thruster is fired for the duration of 200μs. All of these contribute to minimizing both the plasma interaction with downstream neutrals, and the plasma interaction with the vacuum chamber walls. The mean free path for ionization is:

$$\mathrm{mfp} = \frac{1}{n\sigma} \tag{3.1}$$

where n is the neutral gas density and σ is the cross section for ionization. The ideal gas law is used to determine the neutral and argon densities downstream:

$$p = nkT \tag{3.2}$$

For the pressure of 2×10^{-6}Torr, and room temperature, this gives the downstream neutral density of $7.08 \times 10^{16}\mathrm{m}^{-3}$. From literature, the peak ionization cross section for Argon is $4 \times 10^{-19}\mathrm{m}^2$.[27] The mean free path for ionization is 38m, which is far larger than the length and diameter of the chamber. Therefore there are no significant ionizations occurring downstream. The peak electron-neutral collisional cross section is around $1\times10^{-19}\mathrm{m}^2$, which results in a mean free path of 153m. Similarly, the peak ion-neutral collisional cross section is $8 \times 10^{-19}\mathrm{m}^2$, which gives the mean free path of 17m. Since the mean free paths for both electron-neutral and ion-neutral collisions are larger than the length and diameter of the chamber, neither of these interactions will take place inside the chamber, making the environment inside of the vacuum chamber "space-like."

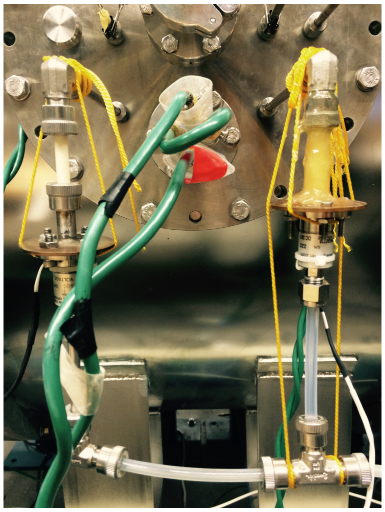

Figure 3.3: Gas Puff Gate Valves

The same neutral injection and ignition system was used from the system used by Prager.[28] Neutral Argon gas flows through the tube (outer diameter of 6.3mm) from the Argon tank to the gas puff gate valves (Parker, P/N 009-1669-900). As pictured in figure 3.3, the gas puff gate valves regulate the amount of gas that flows into the chamber. The pressure of the Argon gas flowing from the tank is set at 20-30psi, and the gas puff gate valves are opened for 4-9ms. After the gas puff gate valves are opened, the neutral Argon gas then flows into the helicon antenna through an alumina tubing with outer diameter of 6.3mm. This necks down to 3.2mm then back to 6.3mm near the gas exhaust end, where the igniter is located. This design resulted in the highest density plasma in the helicon antenna, and alumina was chosen to electrically isolate the igniter from the rest of the tubing.

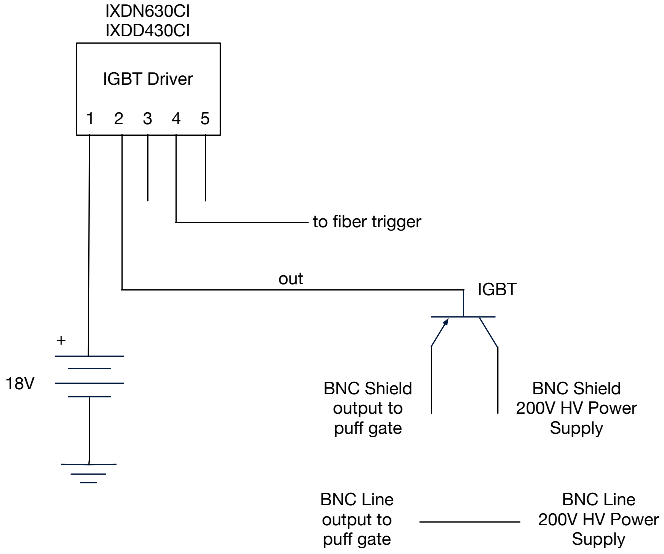

Figure 3.4: Gas Puff Controller Circuit Diagram

As shown in figure 3.4, the main component involved in the gas puff gate controller circuitry is the IGBT and the IGBT driver chip. This puff gate controller circuit is connected to the Model 890A Power Supply, which outputs 200V, and to the gas puff gate valves that are mounted on the side of the vacuum chamber (figure 3.3).

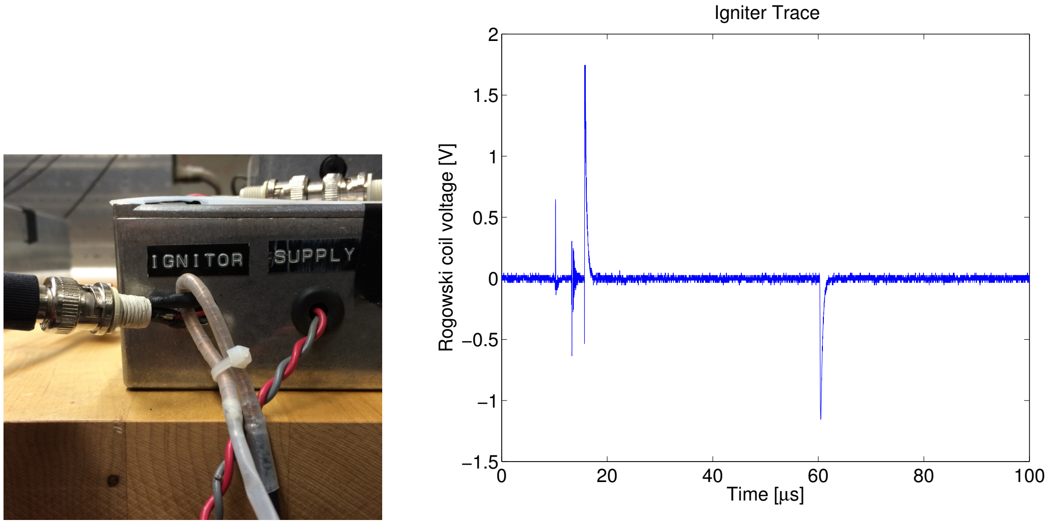

(a) Rogowski coil on igniter circuit

(b) Igniter trace

Figure 3.5: Igniter circuit setup outside of the vacuum chamber and the output from Rogowski coil

The igniter controller circuit follows the same design as the puff gate controller circuit. The difference is that for the igniter controller circuit, the high voltage that is being supplied to the circuitry is 1.5kV. As shown in figure 3.5(a), a miniature Rogowski coil is placed in between the BNC line and shield cable that is connected to the igniter leads. The Rogowski coil is connected to the Tektronix TDS3034 oscilloscope, and the igniter discharge status is monitored throughout the data acquisition. The details of the data acquisition system is discussed in detail in section 3.6, including the Rogowski coil output. The igniter leads are mounted on the side of the chamber via feed through connector. Figure 3.5(b) shows the igniter discharge trace. The spike nearest to 20μs and at 60μs correspond to the beginning and end of pulse. This trace is outputted to the oscilloscope for every shot to verify that the igniter has been successfully discharged. 50Ω voltage terminators are used on the oscilloscope end to reduce the maximum voltage.

3.4 Helicon Antenna and Fast Switching IGBT Power Supply

Figure 3.6: Left handed Nagoya Type III helicon antenna

Following the result from Roberson et al.[24], the Nagoya Type III helicon antenna that is twisted left-hand in space was used. This antenna is designed to excite the m = +1 helicon mode. As shown in figure 3.6, the antenna is 7cm in diameter, 15cm in length, and made out of flat braided wire wound around the quartz tube. Flat braided wire is 5mm in width, and is wound twice around the outside of the quartz tube. The braided wire was chosen for its flexibility, which made it easy to wind in a helical shape around the quartz tube.

$$V(t) = L\frac{dI}{dt} \tag{3.3}$$

The wire is wound twice to increase the current flown through the antenna, and also to increase the inductance through the antenna. From the above equation, both increased current and inductance result in increased voltage through the antenna. In order to prevent arcing, each layer of helical winding is insulated by 3 layers of Kapton® tape. When the antenna is installed into the Double Gun thruster, one end of the quartz tube is closed with a circular quartz plate covered with boron nitrite. The circular quartz plate also has a hole to allow for the igniter and bass puff line to be inserted ∼5cm into the quartz tube. The other end of the quartz tube is left open to allow the plasma to flow out of the thruster. The leads coming out from the antenna is connected to the power supply, which is located outside of the vacuum chamber, via feed through connection mounted on the vacuum chamber flange.

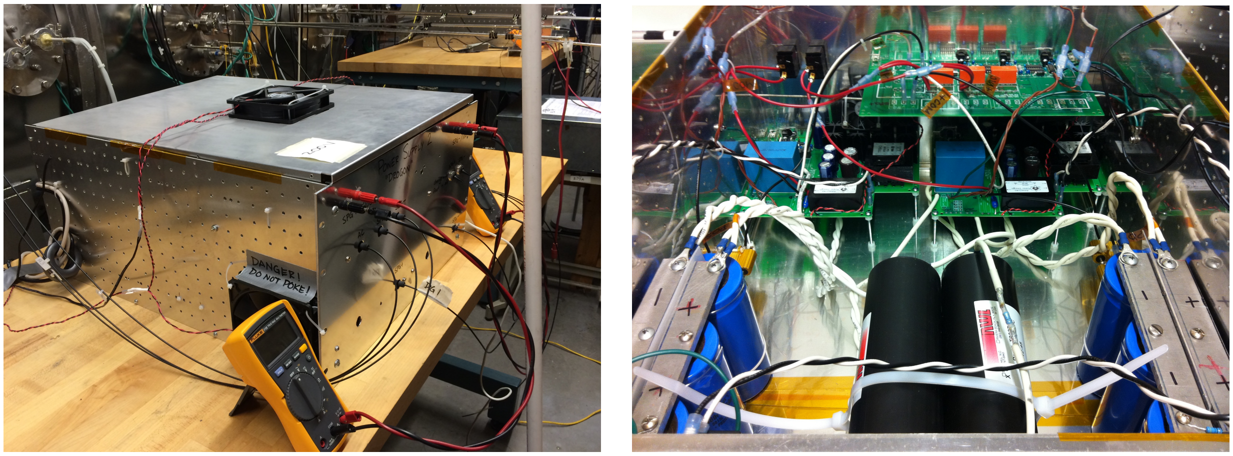

(a) External view (b) Internal view

Figure 3.7: External and internal view of helicon antenna power supply

Figure 3.7(a) shows the overall setup of the helicon antenna power supply. Fiberoptic cables run from the boards to the pulse generator and data acquisition boards, which will be discussed in detail in section 3.6. The multimeters are used to display the voltages of charging capacitors. The fans are placed to avoid overheating the circuit boards inside of the power supply. For safety precaution, the discharge stick (the long white stick in the figure) is attached to the ground end of one of the charging capacitors. This allows us to safely discharge the capacitors in the unlikely scenario that the power supply malfunctions in a manner such that the charging capacitors cannot be discharged electronically.

Figure 3.7(b) shows the internal components of the power supply that is used to drive the antenna to a peak-to-peak current of 1.5kA with peak-to-peak antenna voltage 6-10kV at a frequency of 625kHz. In order to avoid wall effects, the antenna is turned on for 200μs. The set of capacitors along the sides of the box is the charging capacitors with maximum charging voltage of 300V. The set of capacitors at the center is the tuning capacitors for the helicon antenna, which capacitance is set to be 36nF. The inductance and tuning capacitance are estimated from the following equation.

$$2\pi f = \frac{1}{\sqrt{LC}} \tag{3.4}$$

The inductance and tuning capacitance for each thrusters are designed in a way such that both Right and Left Guns are tuned at the same frequency.

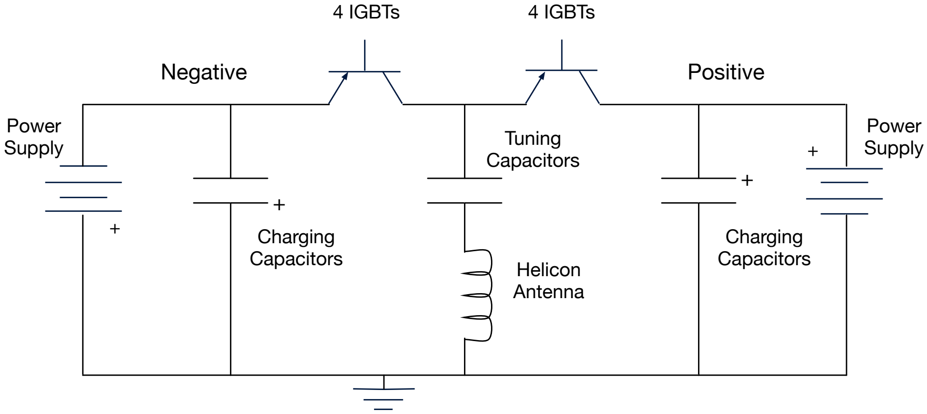

Figure 3.8: Helicon antenna power supply circuit diagram

Figure 3.8 shows the most important components in the helicon antenna power supply circuit. “Positive” refers to the one side of the H-bridge, and “Negative” refers to the other side. The antenna is placed inside of the chamber via feedthrough connection. Physically, “Positive” and “Negative” refers to the two circuit boards placed at the bottom of the power supply box (figure 3.7). These two boards are Seed Plasma Generator boards designed by Eagle Harbor Technologies, Inc., and their main function is the fast IGBT switching – thus able to input a very large amount of power into the helicon antenna.

Figure 3.9: Stangenes Current Transformer

The 0.01 V/A current transformer by Stangenes Industries, Inc. (figure 3.9) is placed across the helicon antenna (figure 3.8) to measure the peak-to-peak current of the helicon antenna. The current trace for each shot is displayed on the Tektronix TDS3034 oscilloscope. The details of the peak-to-peak current trace is discussed in section 3.6.

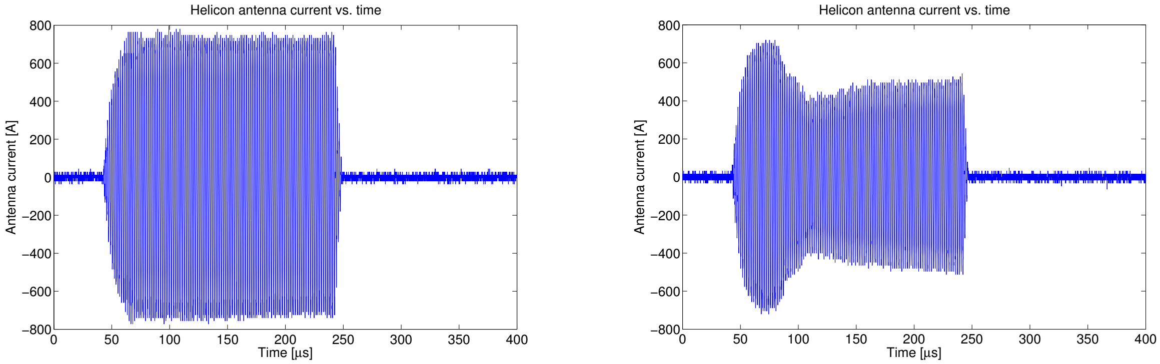

(a) No plasma loading

(b) Plasma loading

Figure 3.10: Helicon antenna trace

Figure 3.16 shows the helicon antenna trace with and without plasma loading. BNC Model 565 Pulse Delay Generator is used to create a pulse wave that is calibrated to be in oscillation with the helicon antenna. For Double Gun thruster, the calibrated frequency is 625kHz. The pulse lesngth is set at 200μs for every shot that is recorded. This short pulse length ensures that the electrons and ions are not colliding with the vacuum chamber wall when the data is collected, thus simulating the space-like environment in the chamber. This trace is also outputted to the oscilloscope for every shot to verify the successful plasma production over the course of the pulse length. As a equipment safety precaution, 50Ω voltage terminators are used for to reduce the maximum voltage.

3.5 Magnetic Coils and Nozzles

Figure 3.11: Double Gun thruster base field magnetic coils and magnetic nozzle

Figure 3.11 shows the top-down view that shows the base field magnetic coils and magnetic nozzles of one of the Double Gun thruster. The base field magnetic coils have inner diameter of 13cm and outer diameter of 22cm. Three base field magnetic coils are used per thruster – 6 total in Double Gun thruster. Magnetic nozzles have inner diameter of 25cm and outer diameter of 28cm. One magnetic nozzle is used per thruster. The helicon antenna is centered inside of the base field magnetic coils, and the plasma ejection end of the antenna is positioned such that it is flush with the base field magnetic coil that is closest to the magnetic nozzle. Figure 3.12 shows the detailed spacing of the base field magnetic coils and a magnetic nozzle. The spacing of 4cm and 5.5cm was chosen, such that the magnetic field around the helicon antenna is kept as uniform as possible, while having a slight increase in magnetic field around the plasma ejection end.

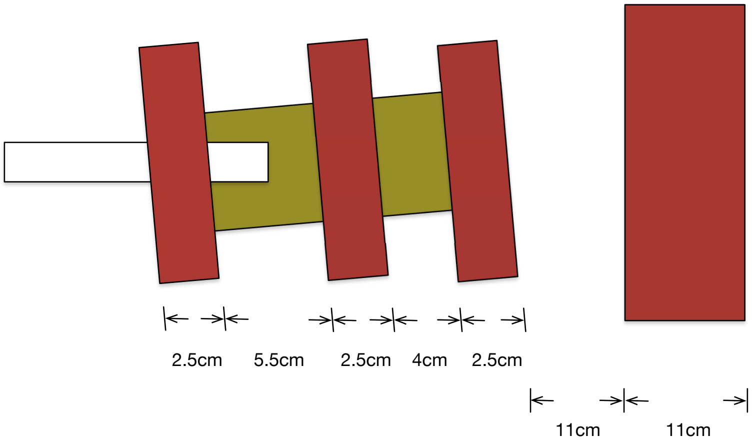

Figure 3.12: Schematic of base field magnetic coils and magnetic nozzle

ASTEX ECR Power Supply (40V, 250A) is used to run a DC current through base field magnetic coils. A separate power supply that was manufactured in-house is used to run a DC current through magnetic nozzles. This power supply is called Pulsed Power Supply, due to its design feature. The circuit is similar in nature to the other electric circuits used in the HPH Double Gun thruster system, where the current oscillation is regulated by IGBT switching. In the case of Pulsed Power Supply, the voltage that is stored in the capacitor bank is discharged when the IGBT closes, in a pulse-like nature.

The F.W. Bell Model 9500 Gaussmeter is used when the vacuum chamber is up-to-air to measure the magnetic field strength generated by both the base field magnetic coils and magnetic nozzles. For base field magnetic coils, the current operating current set at 45A, which gives a magnetic field strength of 162G. For magnetic nozzles, the capacitors in the Pulsed Power Supply is charged to 200V, which corresponds to the magnetic field strength of 105G.

$$B = \frac{\mu_0}{4\pi} \int \frac{I d\mathbf{l} \times \mathbf{r}}{|\mathbf{r}|^3} \tag{3.5}$$

Based on the above Biot-Savart law, the magnetic field of base magnetic field coils and magnetic nozzles for Double Gun thruster is modeled as shown in figure 3.13. The red symbols represent base field magnetic coils, and the green symbols represent magnetic nozzles. The magnetic field is oriented such that it is directed along the flow of the plasma.

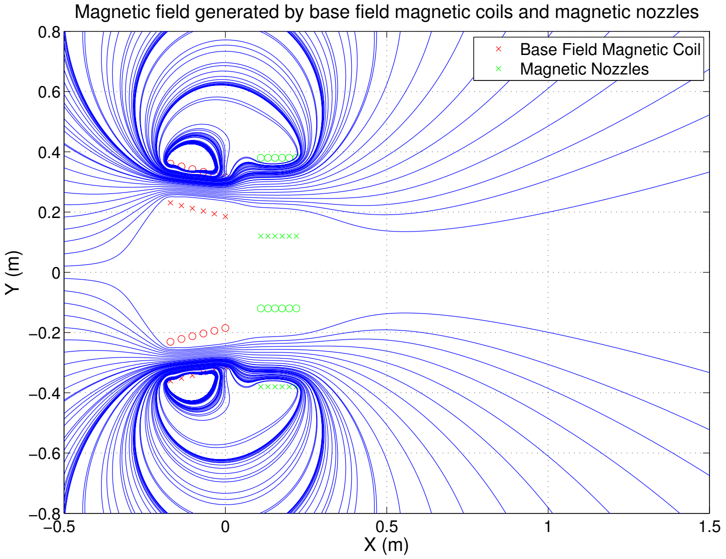

Figure 3.13: Theoretical model of magnetic field

3.6 Data Acquisition

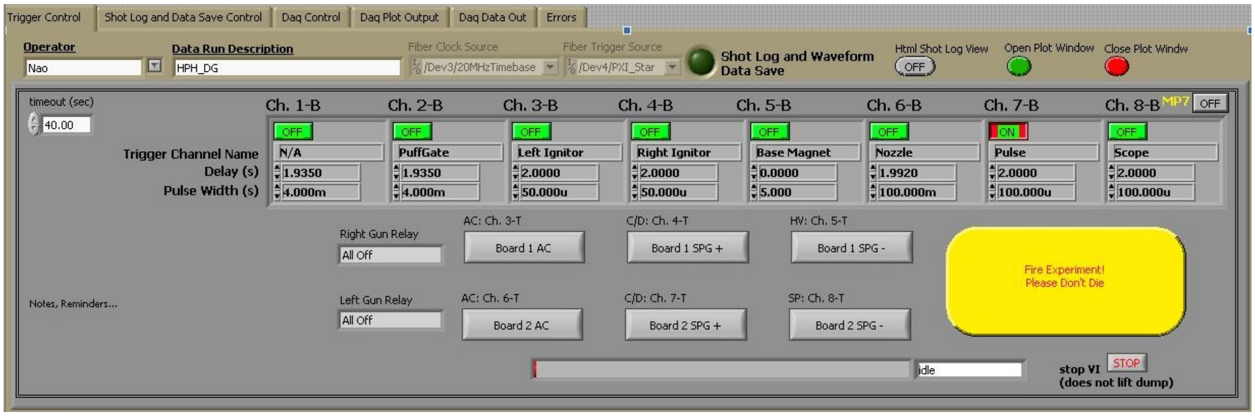

Operator Nao

Data Run Description HPH_DG

Fiber Clock Source /Dev3/20MHzTimebase

Fiber Trigger Source /Dev4/PXI_Star

Html Shot Log View OFF

timeout (sec) 40.00

	Ch. 1-B	Ch. 2-B	Ch. 3-B	Ch. 4-B	Ch. 5-B	Ch. 6-B	Ch. 7-B	Ch. 8-B OFF
	OFF	OFF	OFF	OFF	OFF	OFF	ON	OFF
Trigger Channel Name	N/A	PuffGate	Left Ignitor	Right Ignitor	Base Magnet	Nozzle	Pulse	Scope
Delay (s)	1.9350	1.9350	2.0000	2.0000	0.0000	1.9920	2.0000	2.0000
Pulse Width (s)	4.000m	4.000m	50.000u	50.000u	5.000	100.000m	100.000u	100.000u

Right Gun Relay All Off

Left Gun Relay All Off

idle

stop VI
(does not lift dump)

Figure 3.14: Example of parameters set through LabView VI

LabView is used as a main data acquisition software. It controls the pulse width and duration of the puff gates, igniters, base field magnetic coils, magnetic nozzles, helicon antenna, and, as needed, camera. Figure 3.14 shows the parameters that is being set through LabView. Fiberoptic cables are used to transmit signals to all of the experimental apparatus. Fiberoptic Transmitter FTB8-1000 by Eagle Harbor Technologies, Inc. is used as the interface board. The data to be collected are outputted onto two Tektronix TDS3034 oscilloscopes, which is recorded through LabView, and is converted to text file. This text file is then imported into Matlab for further data analysis.

3.7 Diagnostics – Langmuir Probe

Figure 3.15: Langmuir Probe

Double Langmuir probes are used to obtain the downstream plasma profile and the time of flight data. The probe is very similar in design to the one discussed by Hutchinson.[29] The characteristic of double Langmuir probe is that one probe tip is biased relative to the other probe tip, not relative to the ground. The probe tips are made out of tungsten wire, and have the following dimensions:

- Tip diameter: 1.05mm
- Tip length: 5.04mm
- Tip separation: 2.10mm

They are also carefully filed down to remove any sharp corners that could alter the electric field. The probe tips are connected to magnet wires via a stainless steel crimp, encased in a ceramic housing, and held in place by epoxy. The ceramic housing is attached to the aluminum tube, and the magnet wires run the length of the tube. The aluminum tube is placed at one of the quick disconnect ports alongside the vacuum chamber. The end leads of the magnet wires are connected to a BNC terminal, and connected to the Langmuir probe circuit (figure 3.16(a)).

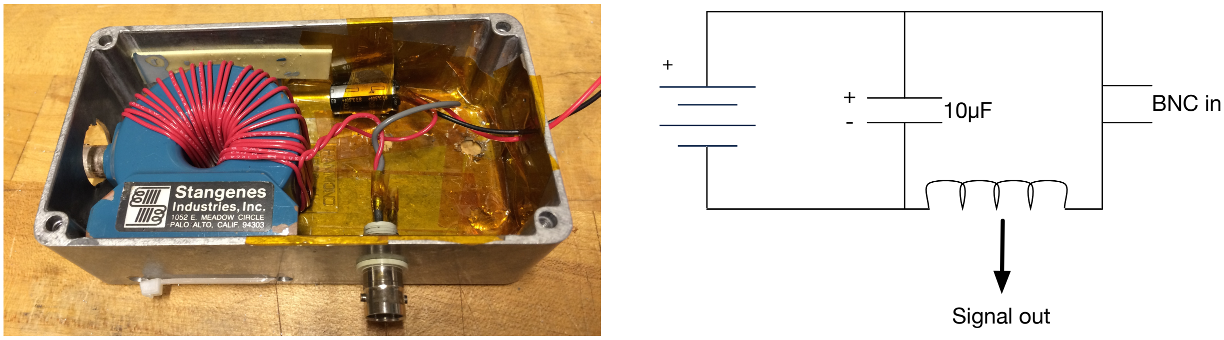

(a) Langmuir probe circuit hardware

(b) Langmuir probe circuit diagram

Figure 3.16: Helicon antenna trace

The bias voltage is applied through a set of batteries in order to isolate the Langmuir probe circuit from RF and electrical noises from other experimental apparatus. The signal is outputted to the oscilloscope through 1 V/A current transformer by Stangenes Industries, Inc. The wire is wound around the Stangenes 25 times, making the voltage-to-current conversion factor 25 V/A. In the previous iterations, the batteries were unable to give off current over the shot length, which is in the order of 100's of μs. The fast acting capacitor was added to the system to alleviate this issue. In order to reduce noise, 150μs RC filter is used on data output line that connects to the oscilloscope.

The traditional usage of Langmuir probe is to place it in the steady flowing plasma. In the case of HPH thruster experiments, the plasma is only treated as steady flowing plasma in the source region. Since the HPH thruster is operated in the pulsed manner, the plasma cannot be treated as a steady flow in the downstream region. RF sources, such as helicon antenna, has an effect of distorting the electron temperature measurement in Langmuir probe.[30] For

HPH Double Gun thruster, the electron temperature is approximated to be 10eV, which is based on the work by Ziemba, et al..[5]

For HPH Double Gun thruster, the downstream plasma density is obtained through the following equation given in Hutchinson.[29]

$$J_i = exp\left(-\frac{1}{2}\right) A_s n_\infty \left(\frac{T_e}{m_i}\right)^{1/2} \tag{3.6}$$

where J_i is the current obtained from Langmuir probe, A_s is the surface area of the probe tip, n_∞ is the plasma density, T_e is the electron temperature, and m_i is the Argon ion mass.

Chapter 4

RESULTS

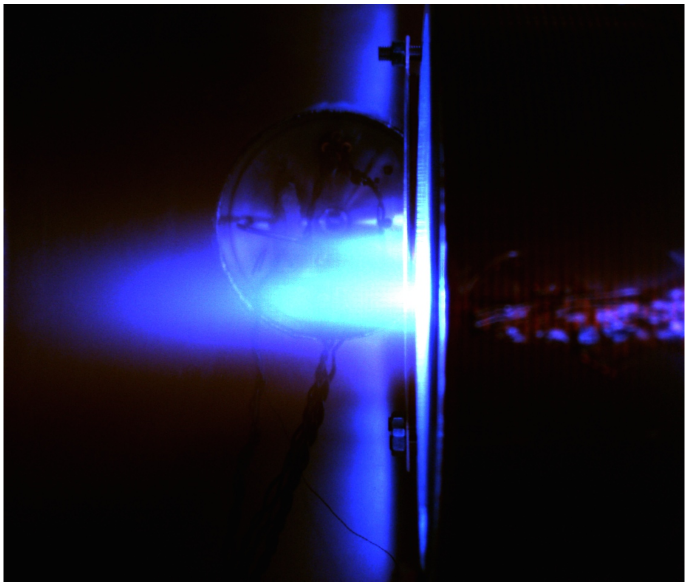

Figure 4.1: Double Gun thruster system firing in the vacuum chamber

This chapter discusses the results obtained from the High-Power Helicon (HPH) Double Gun thruster experiment. Figure 4.1 shows the image of the Double Gun thrusters firing simultaneously in the vacuum chamber. Both camera images and Langmuir data taken over the course of the data collection runs have shown good shot-to-shot repeatability. The radial sweep by Langmuir probe was taken with various axial distances and Langmuir probe orientations. For each radial location, 3 shots were taken. The limitation in shot number is due to several factors. In order to keep the chamber condition as consistent as possible, it is preferable to take the entire radial sweep over the course of a day. It takes on average 15 minutes to take 3 shots per radial location, making that number of shots the most feasible.

Some other limitations include chamber availability, and equipment repair as needed.

4.1 Data Analysis – Theory

While the experimental apparatus is designed to reduce the noise as much as possible, the fact that helicon antennae produces RF waves result in some noise being introduced in the Langmuir probe data. Two digital filtering algorithms are developed and applied to the data to compare the effectiveness of each algorithms.

4.1.1 Fourier Transform

The basic concept of Fourier transform is to literally "transform" the given function back and forth between the physical space, $x \in [-\infty, \infty]$, and frequency space expressed in the form of wavenumber $k = \frac{2\pi}{\lambda}, k \in [-\infty, \infty]$. The Fourier transform equations are:

$$F(k) = \frac{1}{\sqrt{2\pi}} \int_{-\infty}^{\infty} e^{-ikx} f(x) dx \tag{4.1}$$

$$f(x) = \frac{1}{\sqrt{2\pi}} \int_{-\infty}^{\infty} e^{-ikx} F(k) dk \tag{4.2}$$

where equation 4.1 represents the Fourier transform from physical space to frequency space, and equation 4.2 represents the Fourier transform from frequency space to physical space. While the Fourier transform is shown as over the entire real domain of $x \in [-\infty, \infty]$, it is replaced with the finite domain $x \in [-L, L]$ in the computational analysis.

The Fast Fourier Transform (FFT) algorithm is the more computationally efficient way of computing the discrete Fourier transform by reducing the order of operation count to $O(NlogN)$. This reduction in the operation count is achieved by discretizing the domain $x \in [-L, L]$ into 2^n points.

4.1.2 Filter Design

Spectral filtering is most effective when there is just one frequency to be extracted from the data set. By taking the average of the signal in the frequency space over all time shots, the background noise is eliminated. This is because the average of the white noise over several time shots goes to zero. Band-pass filter works by eliminating frequencies that are higher than the frequency set by the filter. In this scenario, band-pass filter is designed around the signal obtained via spectral filtering, which corresponds to the most dominant signal in the Langmuir data. One-dimensional Gaussian filter of the following form is used in this case study.

$$G(k) = exp(-\tau(k_x - k_{x0})^2) \tag{4.3}$$

where τ is the bandwidth of the filter, and k is the wavenumber of the target object.

4.1.3 Singular Value Decomposition

Singular Value Decomposition takes the form:

$$\mathbf{X} = \mathbf{U\Sigma V}^* \tag{4.4}$$

where $\mathbf{V}^* \in \mathbb{C}^{n\times n}$ is a unit matrix that represents rotation, $\mathbf{\Sigma} \in \mathbb{R}^{m\times n}$ is a diagonal matrix that represents stretching, and $\mathbf{U} \in \mathbb{C}^{m\times m}$ is another unit matrix that represents a different rotation. The following figure illustrates the stretch-rotate-stretch concept of SVD.

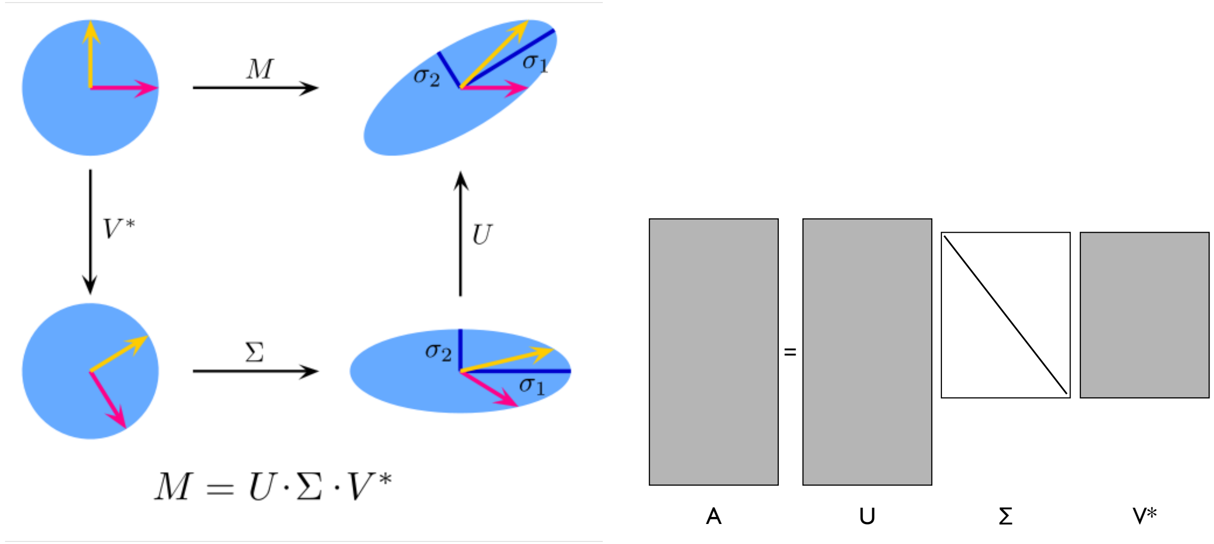

(a) SVD[31]

(b) Matrix representation of SVD[32]

Figure 4.2: Graphic representations of SVD

4.1.4 Principal Component Analysis

In order to extract the principal components from the matrix $\mathbf{X}$, the covariance matrix is expressed as follows:

$$\mathbf{C_X} = \frac{1}{n-1}\mathbf{X}\mathbf{X}^{\mathbf{T}} \tag{4.5}$$

where $\mathbf{C_X}$ is a symmetric square matrix, and the diagonal terms of $\mathbf{C_X}$ are the variances of the $\mathbf{X}$-matrix. Large variances correspond to the dominant signal, and small variances correspond to the noise of the data set, $\mathbf{X}$. The off-diagonal terms of $\mathbf{C_X}$ correspond to the covariance of the $\mathbf{X}$-matrix. Large covariances indicate that there is a close relationship between the data sets (i.e. – redundant data), and small covariances indicate that the data sets are independent of each other (i.e. – not redundant data). Equation 4.5 can be rewritten as follows to be consistent with the SVD variables:

$$\mathbf{C_X} = \frac{1}{n-1}\mathbf{\Sigma^2} \tag{4.6}$$

where the diagonal terms of $\mathbf{\Sigma^2}$ are the variances.

4.2 Data Analysis – Algorithm

4.2.1 Pre-Processing the Data

The data is recorded in the form of two-column .txt file, where the first column represents the time and the second column represents the Langmuir voltage reading. When the data is loaded, the first column is multiplied by 10^6 to scale the data such that the unit is in μs. The second column is multiplied by $-\frac{10^3}{25}$ to convert the unit from voltage to current in mA. The negative sign takes into account for the probe reading that registers positive voltage as negative, and vice versa. The factor of 25 comes from the 1:1 transformer that is placed in the Langmuir probe circuit that gives the conversion factor of $25\frac{V}{A}$. The offset in current reading is subtracted from the entire data set by averaging the first 875 data points. This corresponds to the first 35μs of the data where there is no plasma present, and the current reading is set to zero.

4.2.2 FFT & Gaussian Filter Method

The frequency space is generated, and the FFT of a Langmuir current data is taken for every shot data to determine the dominant frequency. A Gaussian filter (equation 4.3) with the following parameters are designed to extract the signal corresponding to the plasma.

$$\tau = \frac{1}{10000 * [\text{Sampling Frequency}]} \tag{4.7}$$

$$k_0 = 0 \tag{4.8}$$

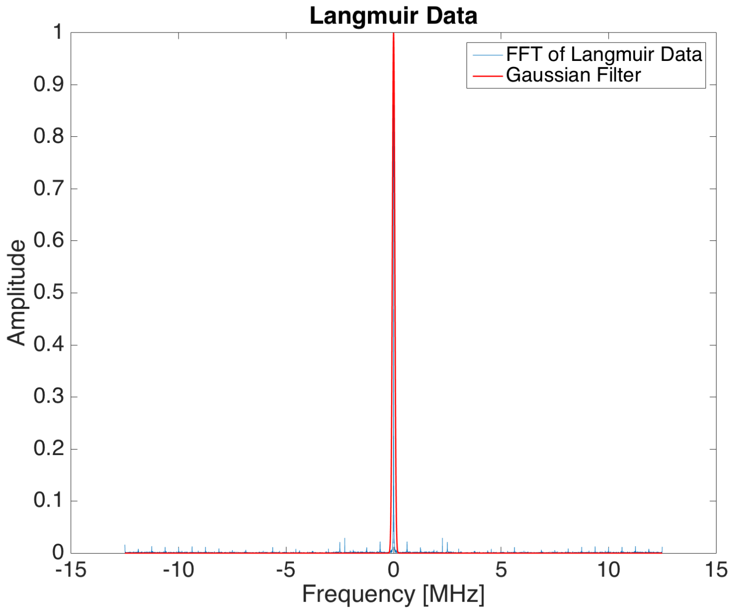

Figure 4.3: FFT of Langmuir data and Gaussian filter designed around the signal

As shown in the above figure, Gaussian filter is applied to the Langmuir current data in frequency space. **An interesting thing of note is that the majority of the noise spikes are harmonics of helicon antenna frequency (625kHz), which indicates that the noise in the Langmuir data is caused by helicon antennae.**

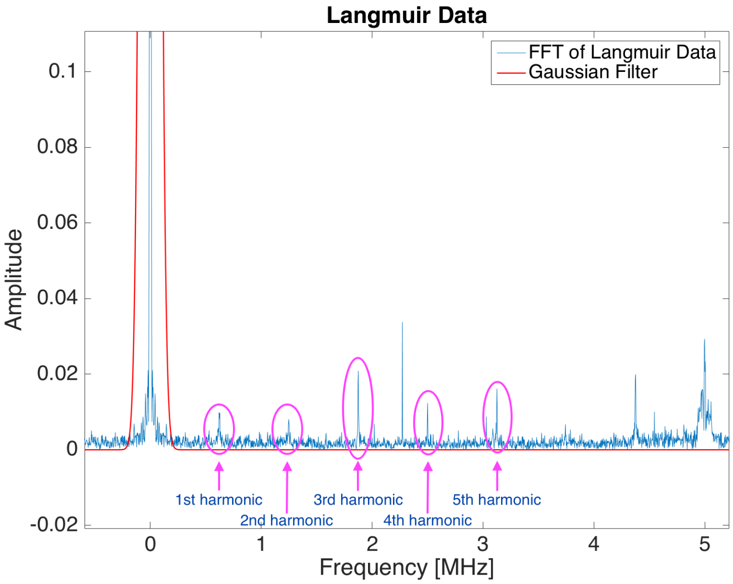

Figure 4.4: Zoomed in version of figure 4.3

The inverse of FFT is taken to bring the current data back into the time space. The plasma arrival time is defined as the first crossing of $95 - 100\%$ of the maximum current value. There are at least three data shots taken per radial location, which is incremented by 5cm over the space of [-30cm, 40cm]. The plasma arrival time is determined in this manner for all shots taken at each radial location. The average of the plasma arrival time is taken over the data set for each radial location.

4.2.3 SVD & PCA Method

The same pre-processing algorithm as described in the previous section was performed. For all shots taken at each radial location, the Langmuir current data is assigned as rows in a matrix $\mathbf{X}$, and SVD is performed on $\mathbf{X}$. As shown in the figure below, the result from SVD on all data sets indicated that the first singular value is much larger than the rest.

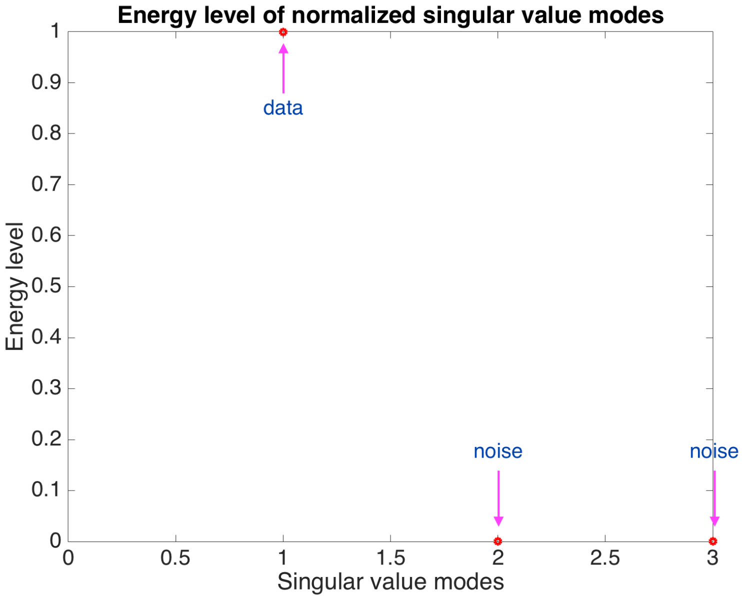

Figure 4.5: Energy level of normalized singular value modes

The Langmuir current data is reconstructed as rank-1 reduced order data by setting all but the first singular values to zero.

$$\mathbf{X}' = \mathbf{U\Sigma V}'^{*}\sqrt{n-1} \tag{4.9}$$

where $\mathbf{V}'^{*}$ is the complex conjugate of $\mathbf{V}$. The average of the rows of this reconstructed Langmuir current data is taken to determine the average amplitude for the data set. Then the FFT of this averaged Langmuir current data is taken, the band-pass filter is applied, and the inverse FFT of the filtered current data is taken to bring it back to the time space. The algorithm for the FFT and band-pass filter is the same as described in the above section; except that there is just one data to be considered, since the average of the data was taken PRIOR to performing the FFT. The plasma arrival time is once again defined as the first crossing of $95-100\%$ of the maximum current value.

4.3 Plasma Density Profile

The intent of the data presented in this section is to visualize the plasma density profile downstream of the Double Gun thruster. The set of data presented below was taken at the following vacuum chamber and gas puff conditions:

- chamber background pressure $\sim 7 \times 10^{-6}$torr
- gas pressure: 30psi
- pulse width: 9ms

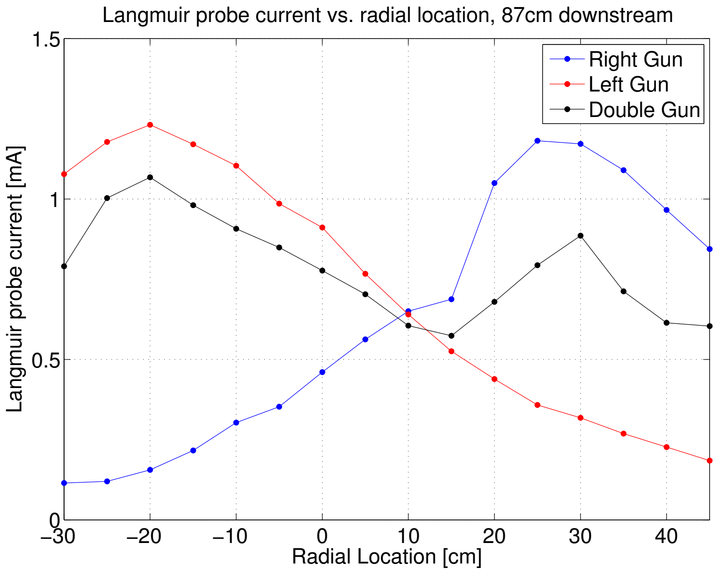

Figure 4.6: Langmuir probe current with varying radial locations with Right, Left, and Double Gun firing at 87cm downstream

Figure 4.6 shows the Langmuir probe current peak values for Right, Left, and Double Gun at varying radial locations at 87cm downstream from the quartz tube. Radial location of +25cm is the centerline of the Right Gun, -25cm is the centerline of the Left Gun, and 0cm is in between Right and Left Guns – the centerline of the Double Gun. This convention applies to all plots presented in this dissertation, and is also illustrated in figure 3.2. FFT and Gaussian filter method was used to extract the signal from the data. Both methods are compared in figure 4.9.

While the Right Gun shows steeper drop off-centerline, the maximum values for Right and Left Guns are comparable at 1.17mA and 1.23mA, respectively. This indicates that the individual HPH thruster performance, in terms of plasma density, is comparable to one another. Double Gun, on the other hand, shows some interesting features. The overall plasma density has decreased from the single firing scheme, which is prominently shown in the decrease in the peak values. The plasma flux, which is evaluated by calculating the area under the curve, immediately downstream for Right Gun is 47.23 mA·cm, Left Gun is 53.77 mA·cm, and Double Gun is 59.24 mA·cm.

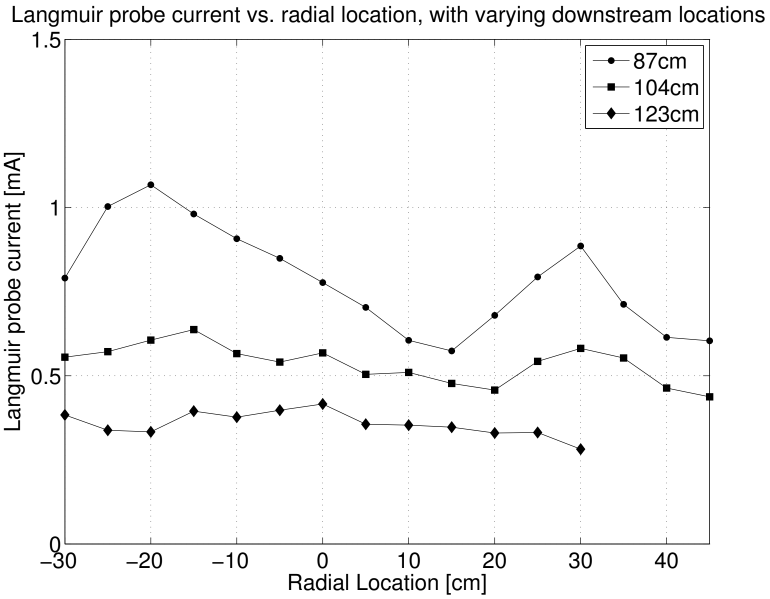

Figure 4.7: Langmuir probe current with varying radial and axial locations with Double Gun firing

In order to visualize how the plasma plume is behaving further downstream when Double Gun is being fired, axial distances of the Langmuir probe were varied. Figure 4.7 shows the Langmuir probe current peak values for the Double Gun system firing simultaneously at varying radial locations at 87cm, 104cm and 123cm downstream from the quartz tube.

The 104cm curve shows the two beams merging into each other, forming a combined plasma plume. Another interesting feature is that the peak value for the Left Gun can now be observed at -15cm, while that for the Right Gun remains at +30cm. Also, a small peak can be observed at 0cm, which is in between the Right and Left Guns. The plasma plume dissipates further downstream, which is shown in the 123cm curve. At this location, there is a slight peak observed at 0cm, and no other distinctive peak can be observed.

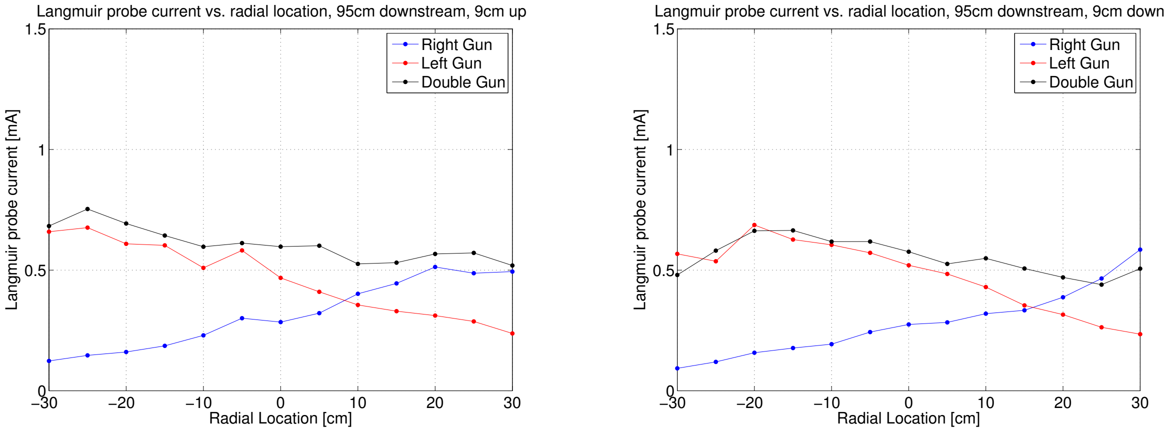

(a) 9cm up

(b) 9cm down

Figure 4.8: Langmuir probe current with varying radial locations at 95cm downstream and ±9cm vertical offset

Figure 4.8 shows the Langmuir probe current peak values for Right, Left, and Double Gun firing with varying radial locations at 95cm downstream from the quartz tube, and at 9cm vertical offset. For the single gun firing scheme, the amount of plasma that is expelled upwards and downwards from the axial centerline is relatively comparable to each other. This is a good indication that the single gun firing scheme is not favoring a certain direction off-axis. For the Double Gun firing scheme, the amount of plasma that is expelled upwards and downwards from the axial centerline is also relatively comparable to each other. This is once again a good indication that the Double Gun system is not favoring a certain direction off-axis.

The total plasma flux for each guns is tabulated below. The total plasma flux for Double

Gun is less than the sum of the total plasma flux from Right and Left Guns. From conservation of flux, this suggests the possibility of increased beam velocity for Double Gun, which will be further discussed in section 4.4.

Table 4.1: Plasma flux for Right, Left, and Double Gun

	Plasma Flux [mA·cm]		
Axial and Vertical Location	Right Gun	Left Gun	Double Gun
87cm downstream, no vertical offset	47.2	53.8	59.2
95cm downstream, 9cm up	18.9	27.9	36.5
95cm downstream, 9cm down	16.5	29.0	33.5
Total Plasma Flux	82.6	111	129

Due to the improvements to the vacuum chamber and to the gas puff circuitry, the second set of data was taken at a later time with the following improved chamber conditions:

- gas line pressure: 20psi
- delay: 1.935s
- pulse width: 4ms

Both the decreased chamber background pressure and the reduced propellant mass should contribute to further increase in the beam velocity, which is discussed in detail in section 4.4.

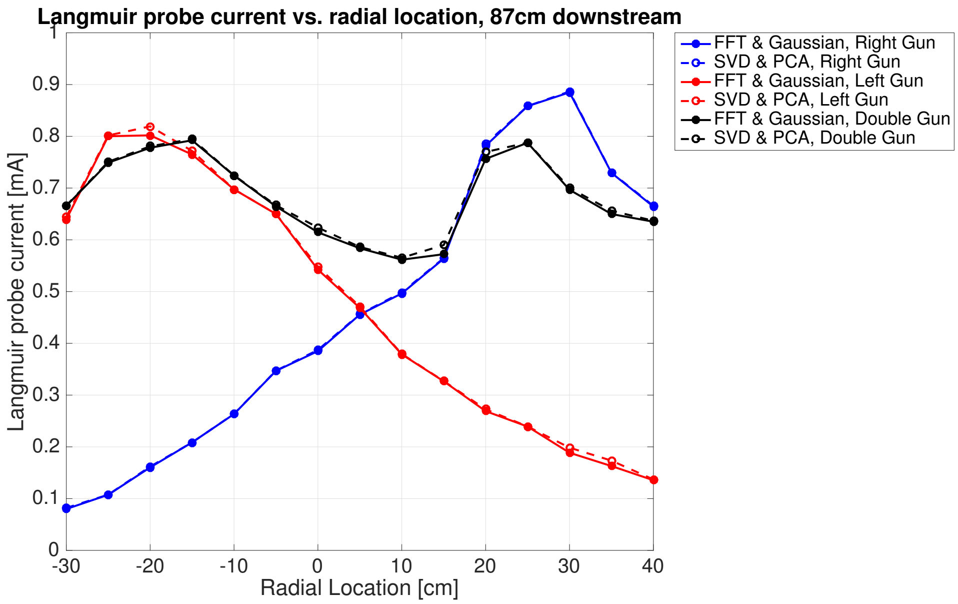

Figure 4.9: Langmuir probe current with varying radial locations with Right, Left, and Double Gun firing at 87cm downstream, with improvements in chamber conditions

Figure 4.9 shows that the overall plasma density has decreased from figure 4.6, which is consistent with the reduced propellant mass. Figure 4.9 also shows that both methods of data analysis – FFT & Gaussian filter and SVD & PCA – are both effective methods to extract signal from a noisy data. Right and Left Gun peak values are more identical at 0.888mA and 0.809mA, respectively. Another interesting feature is that the reduction in plasma density for Double Gun is not as prominent as the previous case. The change in plasma flux for those two chamber conditions are tabulated below for comparison. The plasma flux for Right and Left Gun is also close to being identical at 33.4 and 33.8 mA·cm, respectively, further confirming that Right and Left Gun are operating more identically at the new and improved vacuum chamber condition. Since the propellant mass is decreased, the one-to-one correlation cannot be made to infer the change in plasma density for Double Gun. As such, a relative percentage value is calculated by dividing the plasma flux of Double Gun by the sum of the plasma flux of Right and Left Gun. For the chamber parameter of 7×10^{-6} torr, 30psi, and 9ms puff length, plasma flux for Double Gun is 58.6% of the sum of plasma flux of Right and Left Gun. For the improved chamber parameter of 1.7×10^{-6} torr, 20psi, and 4ms puff length, plasma flux for Double Gun is 71.9% of the sum of plasma flux of Right and Left Gun, which translates to 13.3% increase.

Table 4.2: Plasma flux for Right, Left, and Double Guns at 87cm downstream with different chamber conditions, with ratio of plasma flux for Double Gun and the sum of Right and Left Guns

	Plasma Flux [mA·cm]			
Chamber Parameter	Right Gun	Left Gun	Double Gun	$\frac{\text{Double Gun}}{\text{Right + Left Guns}}$
7×10^{-6} torr, 30psi, 9ms puff length	47.2	53.8	59.2	58.6%
1.7×10^{-6} torr, 20psi, 4ms puff length	33.4	33.8	48.3	71.9%

4.4 Time of Flight

Time of flight data was taken through the following method. The Langmuir probe measurements at 87cm and 104cm downstream was taken with 5cm increments in radial direction. The difference between the time at which the peak value occurs at 87cm and 104cm is taken for the Right, Left, and Double Gun firings, and consequently, the exhaust velocity can be estimated. Following the format from section 4.3, two sets of time of flight data is included, with two varying vacuum chamber and gas puff parameters. The first set of parameters is as below:

- chamber background pressure $\sim 7 \times 10^{-6}$torr
- gas line pressure: 30psi
- pulse width: 9ms

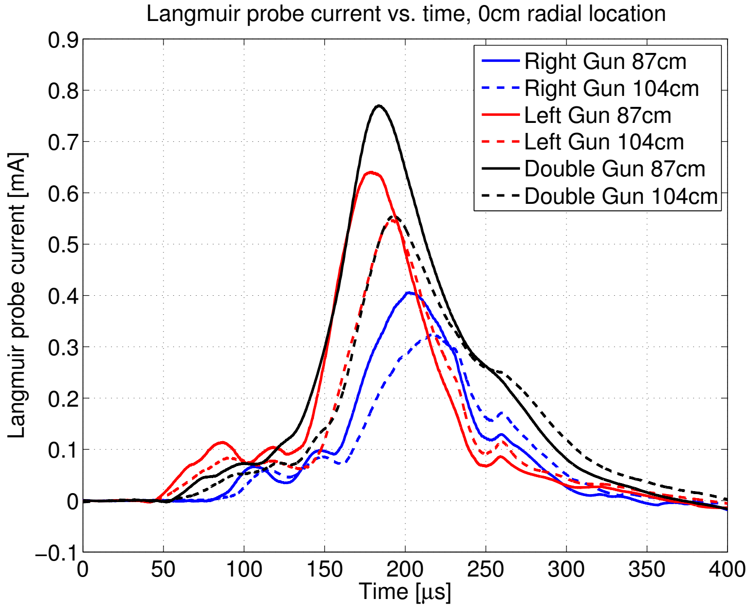

Figure 4.10: Langmuir probe current at 0cm radial location with Right, Left, and Double Gun firing at 87cm and 104cm downstream

Figure 4.10 shows individual Langmuir probe current traces for Right, Left, and Double Gun firings. The measurements taken at 87cm downstream is shown in solid lines, and the traces taken at 104cm is shown in dashed lines. A discrepancy in the plasma density trend can be observed between this figure and Figure 4.6. Because this data set was obtained over the course of 2.5 months, this discrepancy can be attributed to the slight variation in the vacuum chamber and the data acquisition parameters.

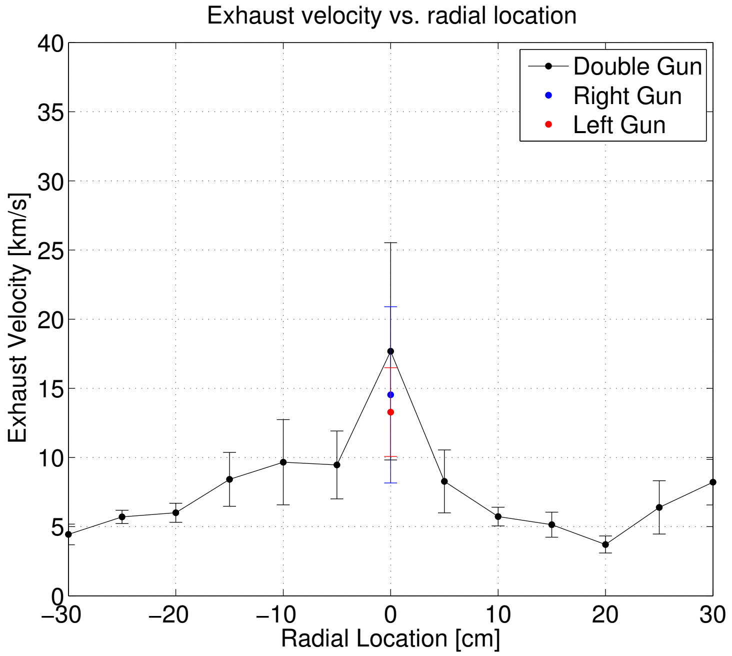

Figure 4.11: Exhaust velocity at varying radial location with Right, Left, and Double Gun firing

Figure 4.11 shows the velocity of the Right Gun firing is 14.5 km/s, and the Left Gun firing is 13.3 km/s. Meanwhile, the velocity of Double Gun system firing simultaneously is 17.7 km/s. This is faster than the average velocity of Right and Left Gun firings, which is 13.9 km/s. The high margin of error at 0cm may be caused by the two helicon antenna interacting with the plasma. Due to the vacuum chamber usage limitations, a full radial sweep for Right and Left Gun firings were not obtained for this data set.

The next set of data is taken under the modified chamber parameters, which is reproduced here:

- gas line pressure: 20psi
- delay: 1.935s
- pulse width: 4ms

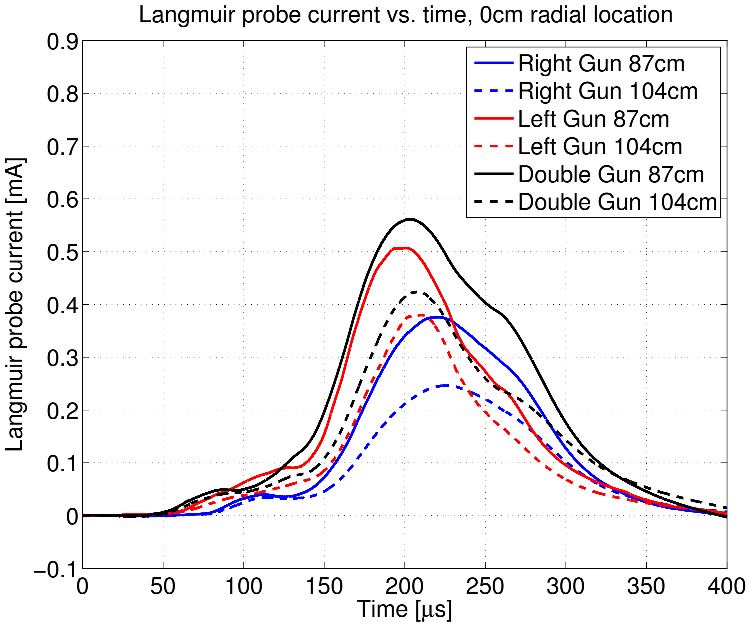

Figure 4.12: Langmuir probe current at 0cm radial location with Right, Left, and Double Gun firing at 87cm and 104cm downstream, with improvements in chamber conditions

Figure 4.12 shows individual Langmuir probe current traces for Right, Left, and Double Gun firings under new vacuum chamber parameters. Unlike the data set represented in Figure 4.10, this data set was obtained in 3 weeks. As such there is no discrepancy in the plasma density trend between Figure 4.12 and 4.9. This in itself emphasizes the importance of data collection over short period of time.

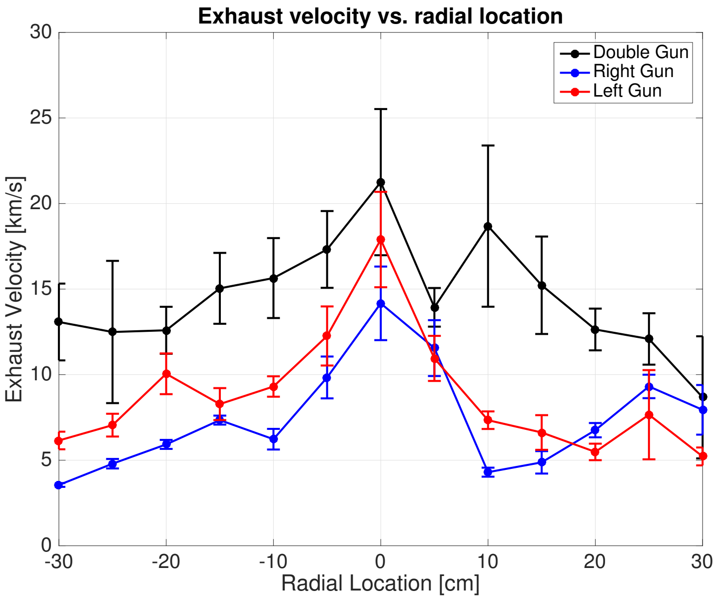

Figure 4.13: Exhaust velocity at varying radial location with Right, Left, and Double Gun firing, with improvements in chamber conditions

Figure 4.13 shows the exhaust velocity profile with varying radial locations. Despite the margin of errors, the exhaust velocities for Right, Left, and Double Guns all increased from the 30psi configuration. One interesting thing of note is that all three thruster configurations have their maximum velocity at 0cm radial location. This aligns with the region of the magnetic field that is directed away from the thrusters (figure 3.13).

Table 4.3 summarizes how the exhaust velocities changed with the chamber parameter. While the Right Gun exhaust velocity remained roughly the same, the Left Gun exhaust velocity increased by 4.5 km/s. The average velocity of the Right and Left Guns is 13.9 km/s for the 30psi configuration, and 16.1 km/s for the 20psi configuration. The Double Gun exhaust velocity for the 20psi configuration is 21.3 km/s, roughly 4 km/s increase from the 30psi configuration. This increase in velocity is due to the lowered background chamber pressure, combined with the reduced gas that is injected into the chamber. Both of these contribute to the reduced neutral collision frequency, which results in increased bulk velocity of the plasma.

Table 4.3: Exhaust velocities for various chamber parameters

	Exhaust Velocity [km/s]			
Chamber Parameter	Right Gun	Left Gun	Average of Right and Left Guns	Double Gun
7×10^{-6} torr, 30psi, 9ms puff length	14.5±6	13.3±3	13.9±5	17.7±8
1.7×10^{-6} torr, 20psi, 4ms puff length	14.2±2	17.9±3	16.1±3	21.3±4

In order to evaluate how well the exhaust velocities from both 20psi and 30psi configurations agree with the scaling law derived in section 2, the average velocity of Right and Left Guns, as well as its minimum and maximum values, are multiplied by $\sqrt{2}$ and compared with the velocity of the Double Gun. The result is tabulated as below.

Table 4.4: Comparison of scaling law and experimental result

	Exhaust Velocity [km/s]	
Chamber Parameter	Scaling Law	Experimental Result
7×10^{-6} torr, 30psi, 9ms puff length	$13.9\sqrt{2}=19.7$	17.7±8
1.7×10^{-6} torr, 20psi, 4ms puff length	$16.1\sqrt{2}=22.7$	21.3±4

In both chamber conditions, the scaled average exhaust velocity of Right and Left Guns are in agreement with the measured exhaust velocity of the Double Gun. Thus the scaling law of downstream exhaust velocity and number of helicon antennae is validated through experimentation. The validity of scaling law is independent of the chamber condition, as long as it is kept constant throughout the set of data.

Chapter 5

SUMMARY AND FUTURE WORK

The Langmuir downstream flow profile and time of flight result indicate that there is a helicon wave interaction when the Double Gun system is fired simultaneously. More precisely, when the Double Gun system is fired simultaneously, the density output decreases, while the exhaust velocity increases in comparison to the single gun firing scheme. The downstream helicon wave propagation theory is derived; it states that the downstream velocity is proportional to square root of the number of helicon antennae used in the system. For the Double Gun thruster system, this corresponds to 41% increase in downstream velocity. The scaling law is validated by comparing the scaled average exhaust velocity of Right and Left Guns with the exhaust velocity of the Double Gun. The scaling law was validated for two different chamber conditions. The varied chamber condition showed that when both the background pressure and the amount of injected gas are reduced, the exhaust velocity would increase as a result due to reduced neutral collision.

In order to test the HPH thruster array system with a magnetic field that is symmetric on all three dimensions, the upgrade of the system from two to four thrusters shall be made, where four plasma beams from HPH thruster array will be directed into the magnetic nozzle. This setup is expected to enhance the beam collimation even more, and to increase the performance of the HPH thruster array system.

Figure 5.1: CAD rendering of HPH thruster array

BIBLIOGRAPHY

[1] Max Light and Francis F Chen. Helicon wave excitation with helical antennas. *Physics of Plasmas (1994-present)*, 2(4):1084–1093, 1995.

[2] Christine Charles and RW Boswell. Laboratory evidence of a supersonic ion beam generated by a current-free ?helicon? double-layer. *Physics of Plasmas (1994-present)*, 11(4):1706–1714, 2004.

[3] Mark Carter, Andrew Ilin, Chris S Olsen, Jared P Squire, and Franklin R Chang Díaz. Using vasimr® for the proposed europa mission. In *AIAA SPACE 2014 Conference and Exposition, San Diego, CA*, 2014.

[4] RM Winglee, P Euripides, T Ziemba, J Slough, and L Giersch. Simulation of mini-magnetospheric plasma propulsion (m2p2) interacting with an external plasma wind. In *39th Joint Propulsion Conference and Exhibition. AIAA Paper*, volume 5225, 2003.

[5] Timothy Ziemba, John Carscadden, John Slough, James Prager, and Robert Winglee. High power helicon thruster. In *41th AIAA/ASME/SAE/ASEE Joint Propulsion Conference, Tucson, AR*, 2005.

[6] R Winglee, T Ziemba, L Giersch, J Prager, J Carscadden, and BR Roberson. Simulation and laboratory validation of magnetic nozzle effects for the high power helicon thruster. *Physics of Plasmas (1994-present)*, 14(6):063501, 2007.

[7] Heinrich Barkhausen. Whistling tones from the earth. *Radio Engineers, Proceedings of the Institute of*, 18(7):1155–1159, 1930.

[8] JA Lehane and PC Thonemann. An experimental study of helicon wave propagation in a gaseous plasma. *Proceedings of the Physical Society*, 85(2):301, 1965.

[9] JP Klozenberg, B McNamara, and PC Thonemann. The dispersion and attenuation of helicon waves in a uniform cylindrical plasma. *J. Fluid Mech*, 21(3):545–563, 1965.

[10] RW Boswell. Very efficient plasma generation by whistler waves near the lower hybrid frequency. *Plasma Physics and Controlled Fusion*, 26(10):1147, 1984.

[11] Francis F Chen. Plasma ionization by helicon waves. *Plasma Physics and Controlled Fusion*, 33(4):339, 1991.

[12] AJ Perry, D Vender, and RW Boswell. The application of the helicon source to plasma processing. *Journal of Vacuum Science & Technology B*, 9(2):310–317, 1991.

[13] PK Loewenhardt, BD Blackwell, RW Boswell, GD Conway, and SM Hamberger. Plasma production in a toroidal heliac by helicon waves. *Physical review letters*, 67(20):2792, 1991.

[14] Francis F Chen. Physical mechanism of current-free double layers. *Physics of Plasmas (1994-present)*, 13(3):034502, 2006.

[15] C Charles, RW Boswell, and MA Lieberman. Xenon ion beam characterization in a helicon double layer thruster. *Applied Physics Letters*, 89(26):261503–261503, 2006.

[16] FR Chang Diaz. An overview of the vasimr engine: High power space propulsion with rf plasma generation and heating. In *Radio Frequency Power in Plasmas: 14th Topical Conference*, volume 595, pages 3–15. AIP Publishing, 2001.

[17] John Vitucci and Raymond Sedwick. Development of a superconducting helicon thruster. In *48th AIAA/ASME/SAE/ASEE Joint Propulsion Conference & Exhibit*, 2012.

[18] JP Sheehan, T Collard, Benjamin W Longmier, and I Goglio. New low-power plasma thruster for nanosatellites. In *50th AIAA/ASME/SAE/ASEE Joint Propulsion Conference*, 2014.

[19] Robert Winglee, John Slough, Tim Ziemba, and Anthony Goodson. Mini-magnetospheric plasma propulsion (m2p2): High speed propulsion sailing the solar wind. In *AIP Conference Proceedings*, number 2, pages 962–967. IOP INSTITUTE OF PHYSICS PUBLISHING LTD, 2000.

[20] Timothy Ziemba, P Euripides, R Winglee, J Slough, and L Giersch. Efficient plasma production in low background neutral pressures with the m2p2 prototype. In *2003, 39th AIAA/ASME/SAE/ASEE Joint Propulsion Conference*, pages 20–23, 2003.

[21] T Ziemba, P Euripides, J Slough, R Winglee, L Giersch, J Carscadden, T Schnackenberg, and S Isley. Plasma characteristics of a high power helicon discharge. *Plasma Sources Science and Technology*, 15(3):517, 2006.

[22] James Prager, Robert Winglee, Tim Ziemba, B Race Roberson, and Gregory Quetin. Ion energy characteristics downstream of a high power helicon. *Plasma Sources Science and Technology*, 17(2):025003, 2008.

[23] James Prager, Timothy Ziemba, Robert Winglee, and B Race Roberson. Wave propagation downstream of a high power helicon in a dipolelike magnetic field. *Physics of Plasmas (1994-present)*, 17(1):013504, 2010.

[24] B Race Roberson, Robert Winglee, and James Prager. Enhanced diamagnetic perturbations and electric currents observed downstream of the high power helicon. *Physics of Plasmas (1994-present)*, 18(5):053505, 2011.

[25] B. Race Roberson. *Experimental Investigation into the Enhanced Diamagnetic Perturbations and Electric Currents Downstream of the High Power Helicon Plasma Thruster.* PhD thesis, University of Washington, 2013.

[26] D.B. Melrose. *Instabilities in space and laboratory plasmas.* Cambridge Univ Press, 1986.

[27] Michael A. Lieberman and Allan J. Lichtenberg. *Principles of plasma discharges and materials processing.* John Wiley and Sons, Inc., 1994.

[28] James Robert Prager. *Experimental Investigation of Plasma Downstream of a High Power Helicon.* PhD thesis, University of Washington, 2008.

[29] Ian H Hutchinson. *Principles of plasma diagnostics.* Cambridge university press, 2005.

[30] Isaac D Sudit and Francis F Chen. Rf compensated probes for high-density discharges. *Plasma Sources Science and Technology*, 3(2):162, 1994.

[31] Georg-Johann. Singular value decomposition, wikimedia commons, https://commons.wikimedia.org/wiki/file:singular-value-decomposition.svg.

[32] J Nathan Kutz. *Data-driven modeling & scientific computation: methods for complex systems & big data.* Oxford University Press, 2013.